JCI The Journal of Clinical Investigation

Macrophage-lineage TRAP+ cells recruit periosteum-derived cells for periosteal osteogenesis and regeneration

Bo Gao, … , Zhuojing Luo, Xu Cao

J Clin Invest. 2019;129(6):2578-2594. https://doi.org/10.1172/JCI98857.

Research Article Bone biology

Graphical abstract

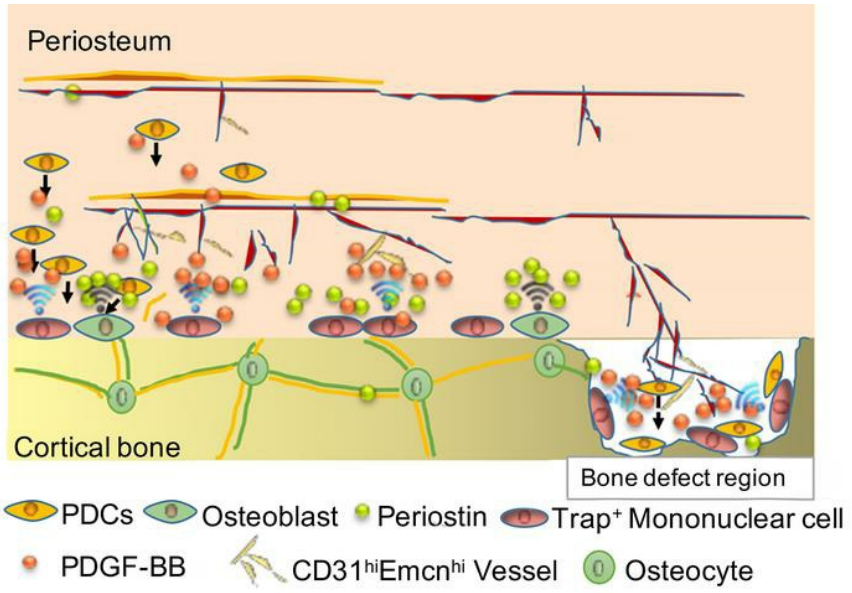

Macrophage-lineage TRAP$^+$ cells recruit periosteum-derived cells for periosteal osteogenesis and regeneration

Bo Gao,[1,2] Ruoxian Deng,[1,3] Yu Chai,[1] Hao Chen,[1] Bo Hu,[1] Xiao Wang,[1] Shouan Zhu,[1] Yong Cao,[1] Shuangfei Ni,[1] Mei Wan,[1] Liu Yang,[2] Zhuojing Luo,[2] and Xu Cao[1]

[1]Department of Orthopaedic Surgery, Institute of Cell Engineering, Johns Hopkins University School of Medicine, Baltimore, Maryland, USA. [2]Institute of Orthopaedic Surgery, Xijing Hospital, Fourth Military Medical University, Xi'an, Shaanxi, China. [3]Department of Biomedical Engineering, Johns Hopkins University School of Medicine, Baltimore, Maryland, USA.

Cortical bones account for more than 80% of human bone mass. The periosteum, a thin tissue that covers almost the entire bone surface, is essential for bone formation and regeneration. However, its osteogenic and bone regenerative abilities are not well studied. In this study, we found that macrophage-lineage cells recruit periosteum-derived cells (PDCs) for cortical bone formation. Knockout of colony-stimulating factor-1 eliminated macrophage-lineage cells and resulted in loss of PDCs with impaired periosteal bone formation. Moreover, macrophage-lineage tartrate-resistant acid phosphatase–positive (TRAP$^+$) cells induced transcriptional expression of periostin and recruitment of PDCs to the periosteal surface through secretion of PDGF-BB, where the recruited PDCs underwent osteoblast differentiation coupled with type H vessel formation. We also found that subsets of Nestin$^+$ and LepR$^+$CD45$^-$Ter119$^-$CD31$^-$ cells (LepR$^+$ PDCs) possess multipotent and self-renewal abilities and contribute to cortical bone formation. Nestin$^+$ PDCs are found primarily during bone development, whereas LepR$^+$ PDCs are essential for bone homeostasis in adult mice. Importantly, conditional knockout of *Pdgfr*-β in LepR$^+$ cells impaired periosteal bone formation and regeneration. These findings uncover the essential role of periosteal macrophage-lineage cells in regulating periosteum homeostasis and regeneration.

Introduction

The periosteum covers almost the entire bone surface and is one of the most regenerative tissues for skeletal osteogenesis (1). Damage to the periosteum severely impairs cortical bone homeostasis (2). The periosteum consists of 2 layers: the inner layer on the periosteal surface with monocyte/macrophage-lineage cells, such as tartrate-resistant acid phosphatase–positive (TRAP$^+$) mononuclear cells, osteoblastic cells, and abundant periostin and the outer layer, which is packed tightly with collagens, blood vessels, and nerve endings (3–6). Periosteum-derived cells (PDCs), also called periosteum-derived multipotent mesenchymal stromal cells (MSCs) (7), periosteal progenitor cells (8), or periosteum-derived stem cells (9), reside distal to the periosteal bone surface and are believed to contain periosteal stem cells (PSCs) that continuously give rise to osteoblasts for osteogenesis (10, 11). A recent study identified a PSC in the long bones and calvarium of mice (12). The periosteum provides a microenvironment that nourishes PDCs to allow underlying periosteal bone formation (13), and periostin is involved in the regulation of periosteum homeostasis (14). PDCs proliferate rapidly and differentiate into various types of cells to support healing after bone fracture (15). This impressive bone regenerative ability of the periosteum has prompted extensive research into the use of PDCs for bone regenerative applications (16–18).

In vitro single-cell lineage analysis has shown that PDCs have mesenchymal multipotency (osteogenic, chondrogenic, adipogenic, and myogenic) at the clonal level and that expanded PDCs can form bone, cartilage, and hematopoietic marrow when transplanted in vivo (19–21). Periosteal cells retain high growth potency and differentiation capability even in elderly patients (22). However, periosteal cell cultures have indicated the heterogeneous nature of PDCs with MSCs, fibroblasts, and osteogenic cells (7). Recently, Chan et al. determined that PDPN$^+$CD146$^-$ CD73$^+$CD164$^+$ expression marks a self-renewing, multipotent human skeletal stem cell, which also resides in the periosteum (23). Using *Ctsk-cre R26R-mT/mG* reporter mice, Debnath et al. found that CD49f^{lo} CD51^{lo}CD200$^+$CD105$^-$ cells in the periosteum are periosteal mesenchymal stem cells (12). These findings indicate that cell markers are essential to characterize the potential stem cell nature of PDCs, which may contain different subpopulations and likely have roles during cortical bone formation and regeneration. MSC activities are progressively enriched in a subset of Nestin$^+$ cells during postnatal life, and Nestin$^+$PDGFR-α$^+$ cells are more similar to primitive bone marrow mesenchymal stromal cells (BMSCs) and are distinct from more differentiated osteoblastic cells (24, 25). Nestin$^+$ cells are abundant in perichondrium, which become the early stage of periosteum during embryonic endochondral ossification (26). Moreover, LepR$^+$ cells, a major subpopulation of MSCs involved in osteogenesis in adults, are very active in response to irradiation or fracture (27, 28). Nestin$^+$ cells and LepR$^+$ cells in the periosteum may

Authorship note: BG and RD contributed equally to this work.
Conflict of interest: The authors have declared that no conflict of interest exists.

Submitted: November 27, 2017; **Accepted:** April 2, 2019; **Published:** May 20, 2019.
Reference information: *J Clin Invest*. 2019;129(6):2578–2594.
https://doi.org/10.1172/JCI98857.

be subsets of PDCs that are responsible for periosteal bone formation. It is imperative to understand how PDCs are involved in the regulation of skeletal osteogenesis and maintaining the periosteum microenvironment.

The periosteum contains cells responsible for cortical bone growth, modeling, remodeling, and bone fracture healing (29, 30). Cortical bone is compact, constituting the "shell" that covers the trabecular bone of vertebrae and long bones (31–33). Cortical bone represents 80% of human bone mass and provides mechanical support of the body and protects vital organs (34). In contrast, the spongy interior trabecular bone that constitutes the remaining 20% of skeletal mass undergoes constant remodeling, primarily for mineral metabolism (35). Our knowledge of bone metabolism and remodeling is based predominantly on the study of trabecular bone. The contribution of cortical bone for peak bone mass is substantial, however, and the risk of bone fracture depends mainly on cortical bone density and strength (30, 36, 37). We have limited understanding of the mechanism of cortical bone formation and homeostasis.

Knockout of macrophage colony-stimulating factor-1 (*Csf1*$^{-/-}$) leads to the depletion of mononuclear phagocytes, including macrophages and TRAP$^+$ cells, and to markedly impaired cortical bone formation (4, 38). Resident macrophages present in various tissues regulate the microenvironment for homeostasis and regeneration (39–41). Although the function of TRAP$^+$ cells is bone resorption, recent studies have shown that TRAP$^+$ cells are signaling-initiated cells that modulate the niche in which they reside (42, 43). We have previously shown that TRAP$^+$ mononuclear cells secrete PDGF-BB to recruit MSCs for osteogenesis, coupled with angiogenesis (4). We have also determined that TRAP$^+$ cells secrete NETRIN-1 to induce sensory nerve axonal growth in subchondral bone (44). Moreover, we found that the TRAP$^+$ cell–mediated release of TGF-β not only induces MSC but also induces the initial pathological changes of enthesopathy (45, 46).

In this study, we investigated the role of periosteal macrophage-lineage cells, particularly TRAP$^+$ mononuclear cells, in maintaining periosteum homeostasis and regulating PDC differentiation for periosteal bone formation. We found that subsets of periosteal Nestin$^+$ and LepR$^+$ cells have the potential to give rise to osteoblasts for periosteal bone formation. Resident macrophage-lineage cells maintain periosteum homeostasis, and TRAP$^+$ mononuclear cells recruit PDCs to the periosteal osteogenic microenvironment for bone formation and regeneration.

Results

Nestin$^+$ and LepR$^+$ PDCs are located in the outer layer of the periosteal surface. To understand the potential role of PDCs, along with abundant matrix proteins and blood vessels in the periosteum to promote cortical bone formation, we performed immunostaining of longitudinal periosteal sections of the tibiae of mice from early postnatal to late adulthood. We found that TRAP$^+$ mononuclear cells were abundant on the periosteal bone surface in young mice and decreased markedly during late adulthood (Figure 1, A, B, and F), whereas few TRAP$^+$ mononuclear cells resided on the endosteal bone surface (Figure 1, A, B, and G). We found very few TRAP$^+$ multinuclear cells on the surface of cortical bone during the early postnatal period, and the cell numbers gradually increased during adulthood (Figure 1H). Notably, periostin was expressed abundantly adjacent to the periosteal bone surface with type H (CD31^{hi}Emcn^{hi}) vessels during cortical bone growth and diminished during late adulthood (Figure 1, C, D, M, and N), suggesting an osteogenic environment at the periosteal surface. The cellularity in the periosteum was seen largely on the periosteal surface and increased continuously until early adulthood, then decreased during late adulthood (Figure 1, E, O, and P). Nevertheless, the large area of periosteum distal to the periosteal surface has far fewer cells, with no periostin or type H vessels and is clearly distinct from the inner layer (Figure 1, C, D, M, and N). Interestingly, periosteal Nestin$^+$ cells and LepR$^+$ cells resided primarily in the outer layer, and Nestin$^+$ cells were abundant in young mice, whereas LepR$^+$ cells were abundant in adult mice (Figure 1, A, B, and I–L).

Subsets of Nestin$^+$ and LepR$^+$ PDCs possess self-renewal and multidifferential potency. To investigate whether Nestin$^+$ and LepR$^+$ PDCs contain potential stem/progenitor cells for cortical bone formation, we tested the multilineage potency and self-renewal of periosteal Nestin$^+$ and LepR$^+$ cells. Cells isolated from the periosteum of Nestin-GFP mice at different ages were analyzed by flow cytometry using GFP in combination with negative selection of CD45, Ter119, and CD31. The mean proportion of periosteal Nestin$^+$CD45$^-$Ter119$^-$CD31$^-$ cells was 0.64% ± 0.11% among all sorted periosteal cells in 1-month-old Nestin-GFP$^+$ mice and decreased significantly to 0.03% ± 0.01% in 3-month-old mice (Supplemental Figure 1A; supplemental material available online with this article; https://doi.org/10.1172/JCI98857DS1). Moreover, 5.4% ± 1.6% of Nestin$^+$ PDCs were positive for LepR in 1-month-old mice, and 9.6% ± 3.5% were positive for LepR in 3-month-old mice, indicating 2 subpopulations of PDCs (Supplemental Figure 1B). It was interesting to note Nestin$^+$ PDCs were 88% ± 3.1% and 93% ± 3.4% positive for MSC markers PDGFR-α and PDGFR-β, respectively (Supplemental Figure 1C). However, only 41% ± 4.8% of PDGFR-α$^+$CD45$^-$Ter119$^-$CD31$^-$ cells were Nestin-GFP$^+$, indicating the different subpopulations of Nestin-GFP$^+$ and PDGFR-α$^+$ cells (Supplemental Figure 1D). Moreover, Nestin$^+$PDGFR-α$^+$ PDCs were highly positive for MSC markers CD90 (81% ± 5.7%) and CD105 (80% ± 3.9%), whereas only 20% ± 3.7% and 20% ± 2.3% of Nestin-GFP$^+$ PDGFR-α$^-$CD45$^-$Ter119$^-$CD31$^-$ cells were positive for these markers, respectively, suggesting that periosteal Nestin-GFP$^+$ cells contain PDGFR-α$^+$ stem/progenitor cells and PDGFR-α$^-$ cells (Supplemental Figure 1, E–H). In a similar experiment using *LepR-cre R26R-EYFP* mice, we found that periosteal LepR$^+$ PDC cells were relatively scarce in 1-month-old mice (0.02% ± 0.01%) and significantly increased in 3-month-old mice (0.52% ± 0.31%), in contrast to Nestin-GFP$^+$ PDCs (Supplemental Figure 1I). LepR$^+$ PDCs were 94% ± 1.2% and 94% ± 2.5% positive for MSC markers PDGFR-α and PDGFR-β, respectively (Supplemental Figure 1J). Remarkably, nearly 93% of PDGFR-α$^+$CD45$^-$Ter119$^-$CD31$^-$ cells were LepR$^+$ (Supplemental Figure 1K). Meanwhile, nearly 83% and 78% of LepR$^+$ PDCs were also highly positive for MSC markers CD90 and CD105, respectively, suggesting that these periosteal cells might be highly enriched for MSCs (Supplemental Figure 1, L–N).

To assess the colony-forming unit–fibroblast (CFU-F) activity, we sorted and expanded different subpopulations of periosteal cells and added them to adherent cultures at clonal density. Results showed the percentage of cells in each cell population sorted from CD45$^-$Ter119$^-$CD31$^-$ periosteal cells that formed CFU-Fs in culture.

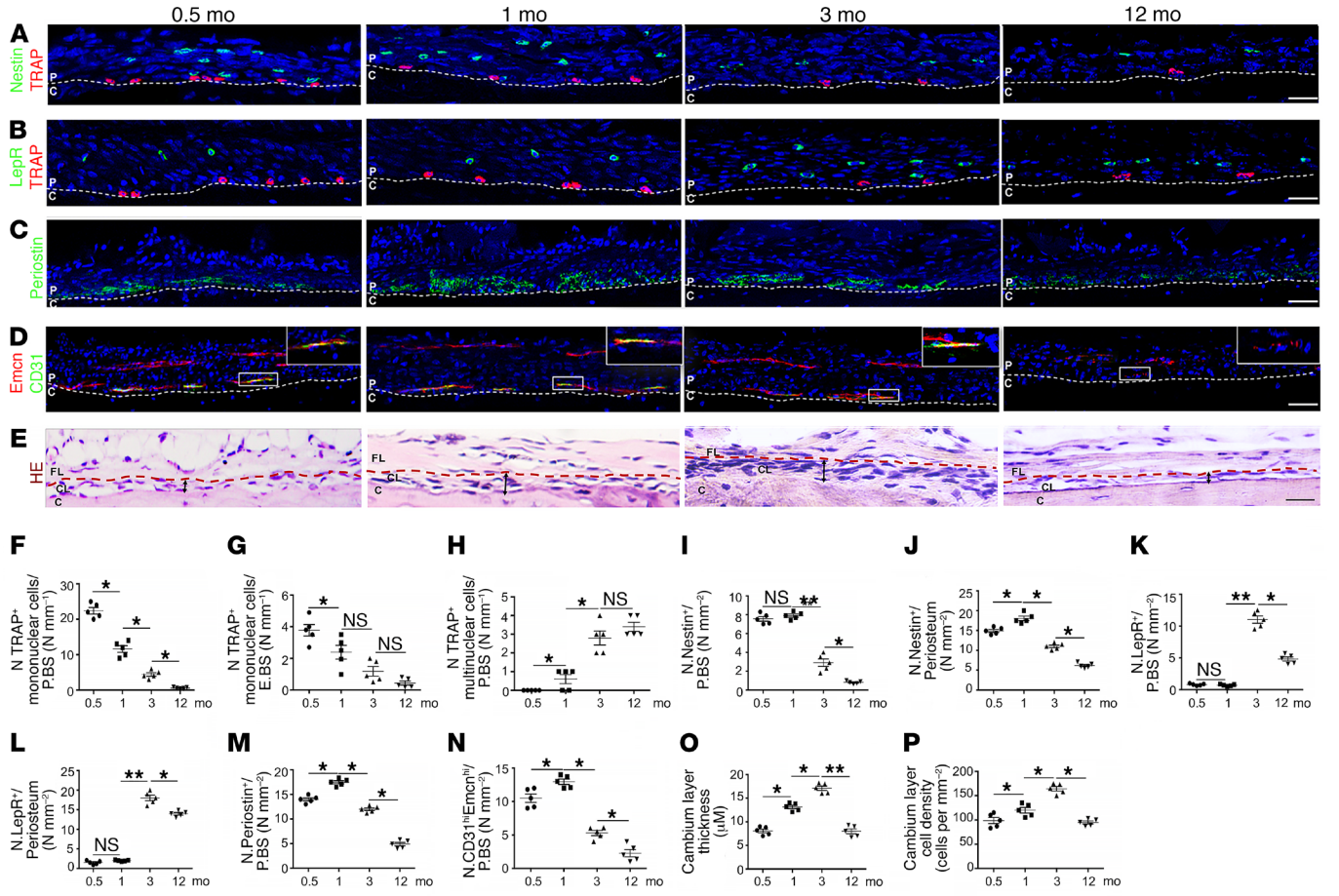

Figure 1. Nestin⁺ and LepR⁺ cells are located in the outer layer of the periosteum. (**A**–**D**) Representative images of coronal tibia diaphyseal periosteum sections from 0.5-, 1-, 3-, and 12-month-old male mice stained for TRAP and Nestin (**A**), TRAP and LepR (**B**), periostin (**C**), Emcn and CD31 (**D**), and representative H&E staining images (**E**). (**F**–**N**) Quantification of the periosteal (**F**), endosteal TRAP⁺ mononuclear cells (**G**), periosteal TRAP⁺ multinuclear cells (**H**), Nestin⁺ cells (**I** and **J**), LepR⁺ cells (**K** and **L**), periostin⁺ cells (**M**), and CD31^{hi}Emcn^{hi} vessels (**N**) in the inner layer of periosteum (no. cells/P.BS) and/or whole periosteum (no. cells/periosteum) (n = 5 mice/group). (**O** and **P**) Quantification of the thickness (**O**) and cellularity (**P**) of the inner layer of periosteum. Scale bars: 100 μm (n = 5 mice/group). Dashed lines in **A**–**D** indicate the limit between the inner layer and outer layer of periosteum and cortical bone. Dashed lines in **E** indicate the limit between the inner layer and outer layer of periosteum. The double-headed arrows indicate the width of the inner layer of periosteum. Data are presented as mean ± SEM. *P < 0.05; **P < 0.01. C, cortical bone; CL, cambium layer (inner layer) of periosteum; FL, fibrous layer (outer layer) of periosteum; NS, not significant as determined by ANOVA with Bonferroni's post hoc analysis.

Nestin-GFP⁺PDGFR-α⁺ PDCs and LepR⁺CD105⁺ PDCs possessed higher CFU-F activity among other cells, indicating a potential subpopulation of Nestin⁺ and LepR⁺ PDCs. Of note, the CFU-F activities between LepR⁺ and LepR⁺CD105⁺ cells were not significantly different, suggesting that most LepR⁺ CFU-Fs in the periosteum were CD105⁺ (Supplemental Figure 1O).

We then measured and compared the self-renewal and multidifferential potency between PDCs and BMSCs by using FACS Nestin⁺ PDGFR-α⁺ CD45⁻Ter119⁻CD31⁻ and LepR+ PDCs cells. Notably, both Nestin⁺PDGFR-α⁺ and LepR⁺ PDCs formed more CFU-Fs than those of BMSCs (Supplemental Figure 2, A, B, and F). Individual CFU-Fs were then split into 3 aliquots in cultures for osteoblast, chondrocyte, or adipocyte differentiation (Supplemental Figure 2, C–E and G–I). Both Nestin⁺PDGFR-α⁺ and LepR⁺ PDCs showed trilineage differentiation ability with more osteogenic and chondrogenic potency than BMSCs (Supplemental Figure 2, G and I), which was confirmed by expression of osteogenesis-related genes (*Osterix*, *Runx2*) and chondrogenesis-related genes (*Col2a1*, *Sox9*) (Supplemental Figure 2, J–L).

Next, CFU-Fs derived from Nestin⁺PDGFR-α⁺ and LepR⁺ PDCs were injected into the femora of 1-month-old NOD SCID mice at a density of 1×10^6 to measure their in vivo self-renewing ability (Figure 2, A and B). GFP⁺ or YFP⁺ cells from the bone marrow were collected by FACS 8 weeks after injection and plated for CFU-F formation. The colonies were expanded and retransplanted into the femora of recipient mice for the second round of in vivo self-renewal assay. Importantly, all colonies generated by the secondary CFU-Fs still highly expressed CD90 (80% ± 2.5% from Nestin⁺PDGFR-α⁺ PDCs and 80% ± 3.2% from LepR⁺ PDCs) and CD105 (74% ± 4.2% from Nestin⁺PDGFR-α⁺ PDCs and 76% ± 5.7% from LepR⁺ PDCs) (Figure 2, A and B). The in vivo self-renewing ability and in vitro multidifferential potency results indicate that subsets of Nestin⁺ and LepR⁺ PDCs might be stem/progenitor cells.

To demonstrate the differentiation of Nestin⁺ and LepR⁺ PDCs for periosteal bone formation, we performed lineage tracing using *Nestin-creERT2 R26R-EYFP* mice by injecting tamoxifen at P14 or P60. The labeled Nestin⁺ cells were analyzed 14 days (2 and 7 days

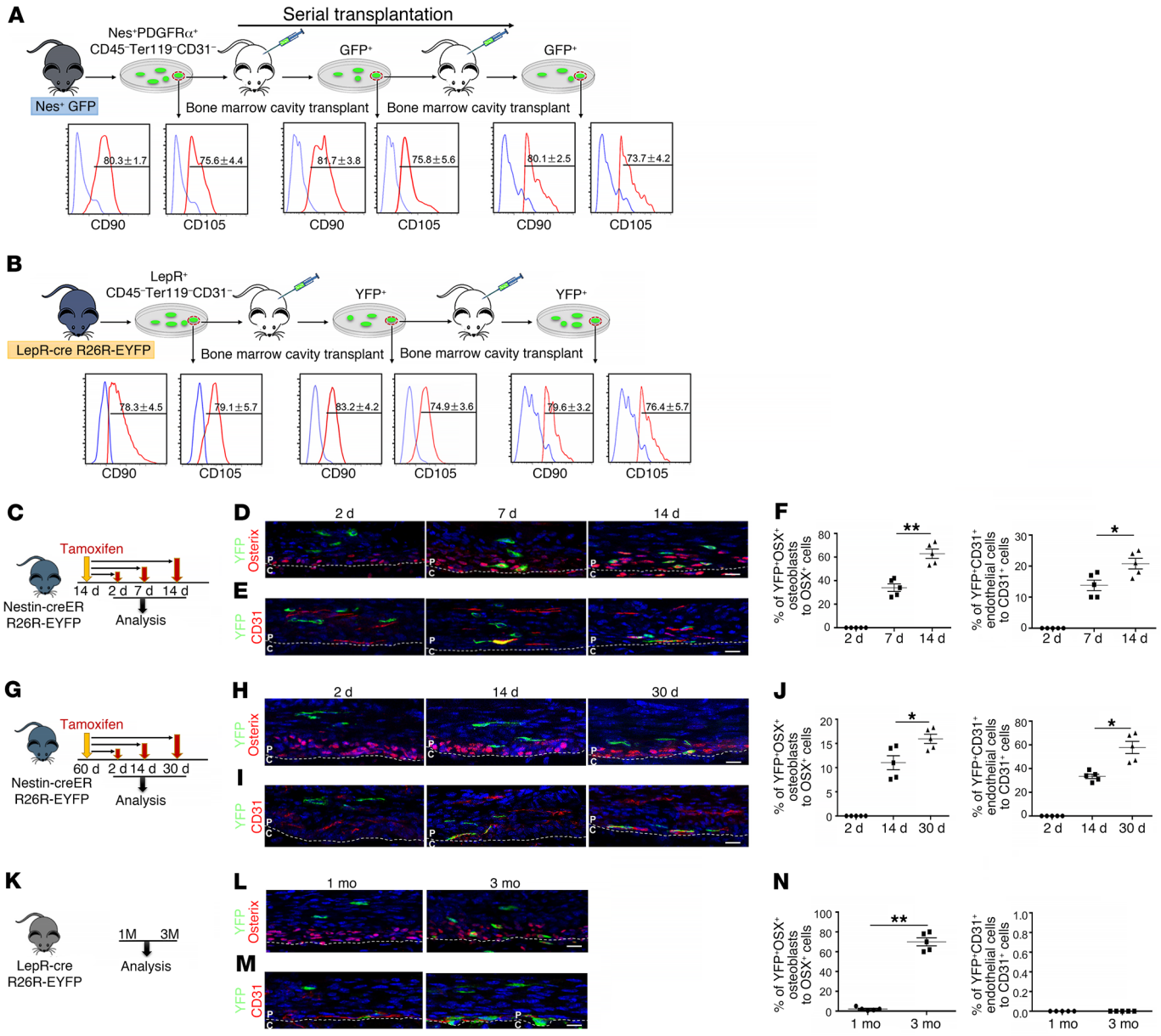

Figure 2. Subsets of periosteal Nestin⁺ and LepR⁺ cells possess self-renewal capacity and commit to osteogenic lineage cells. In vivo serial transplantation of Nestin-GFP⁺PDGFR-α⁺ CD45⁻Ter119⁻CD31⁻ (**A**) and LepR-YFP⁺CD45⁻Ter119⁻CD31⁻ PDCs (**B**). Single cell–derived colonies from donors' PDCs were expanded to generate 5 × 10^6 cells and injected into the femora of five 1-month-old NOD SCID mice at a density of 1 × 10^6 per injection. GFP⁺ or YFP⁺ cells were sorted from the primary recipients' bone marrow at 8 weeks after injection and harvested for forming CFU-Fs. The colonies were then transplanted into the secondary recipient mice. FAC analysis of CFU-Fs showed the percentages of GFP⁺ or YFP⁺ cells expressing MSC markers (CD90 and CD105) (bottom panels in **A** and **B**). (**C**–**J**) Lineage-tracing of periosteal Nestin⁺ cells in *Nes-creERT2 R26R-EYFP* mice. Samples were collected 2, 7, and 14 days or 2, 14, and 30 days after tamoxifen (100 mg/kg i.p.) administration at P14 or P60, respectively (**C**, **G**). Representative images of coronal tibia diaphyseal periosteum sections stained for YFP and Osx (**D** and **H**), YFP and CD31 (**E** and **I**). Quantification of Nestin⁺ lineage cells' contribution to periosteal Osx⁺ osteoblasts (**F** and **J**, left panel), CD31⁺ endothelial cells (**F** and **J**, right panel) (*n* = 5 mice/group). Representative images from 1- or 3-month-old *LepR-cre R26R-EYFP* mice stained for YFP and Osx (**L**), YFP and CD31 (**M**). Scale bars: 20 μm. (**N**) Quantification of LepR⁺ lineage cells' contribution to periosteal Osx⁺ osteoblasts (left panel) and CD31⁺ endothelial cells (right panel). Data are presented as mean ± SEM. **P* < 0.05; ***P* < 0.01. C, periosteal cortical bone; NS, not significant as determined by ANOVA with Bonferroni's post hoc analysis; P, periosteum.

after injection, as controls) or 30 days (2 and 14 days after injection, as controls) after injection (Figure 2, C–J). Coimmunostaining of yellow fluorescent protein (YFP) with Osterix (Osx) or CD31 showed that periosteal Nestin⁺ cells from P14 largely migrated to the periosteal surface, most differentiated to Osx⁺ osteoprogenitors, and a few differentiated to CD31⁺ endothelial cells (Figure 2, D–F). Nevertheless, Nestin⁺ cells from P60 were primarily differentiated to CD31⁺ endothelial cells (Figure 2, H–J). In contrast, we observed almost no coimmunostaining of YFP with Osx in 1-month-old *LepR-cre R26R-EYFP* mice but significantly increased LepR⁺Osx⁺ cells on the periosteal surface of 3-month-old mice (Figure 2L). Moreover, LepR⁺ cells were located adjacent to CD31⁺

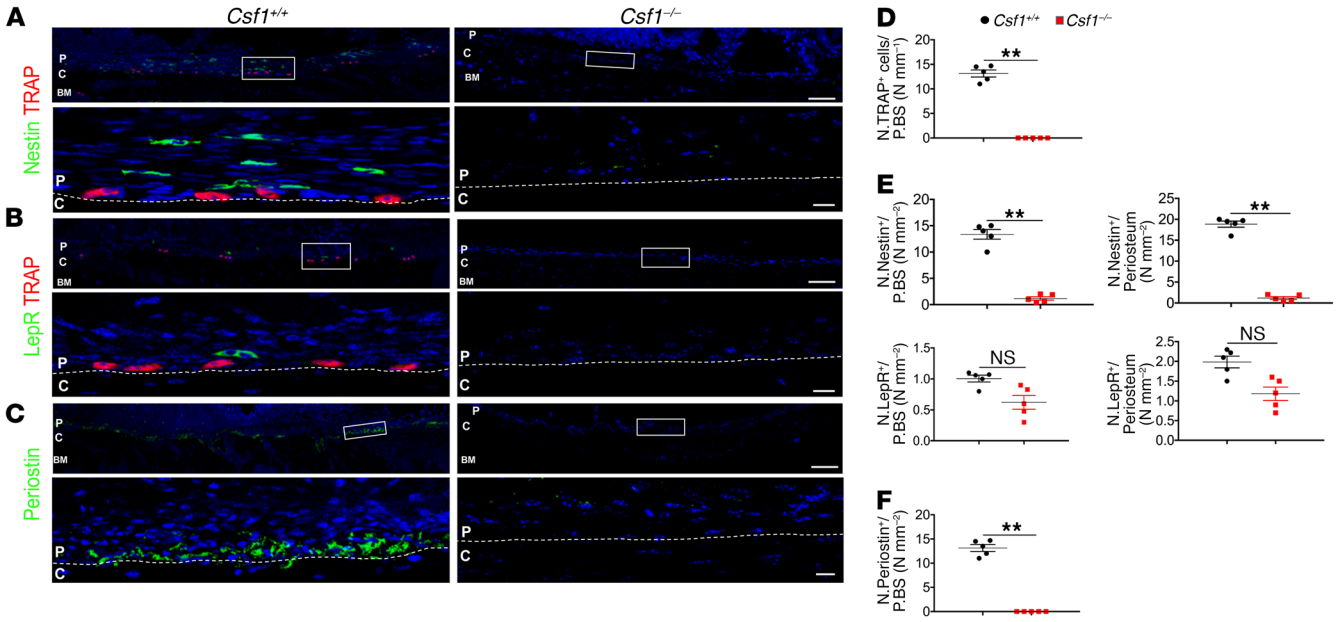

Figure 3. Deficiency in macrophage-lineage cells impairs cortical bone formation and periosteum homeostasis. (**A**–**C**). Upper panels, representative images of coronal tibia diaphyseal periosteum sections from *Csf1*$^{-/-}$ mice and their control littermates (*Csf1*$^{+/+}$) stained for TRAP and Nestin (**A**), TRAP and LepR (**B**), and periostin (**C**). Lower panels, high-power magnification images of the boxed area of the upper panels. (**D**–**F**) Quantification of TRAP$^+$ mononuclear cells (**D**), Nestin$^+$ cells and LepR$^+$ cells (**E**), and periostin$^+$ cells (**F**) in the inner layer of periosteum (no. cells/P.BS) and/or whole periosteum (no. cells/periosteum) (n = 5 mice/group). Dashed lines in **A**–**C** indicate the limit between periosteum and cortical bone. Scale bars: 100 μm (upper panels), 20 μm (lower panels). Data are presented as mean ± SEM. *P < 0.05; **P < 0.01. C, periosteal cortical bone; NS, not significant as determined by 2-tailed Student t test; P, periosteum.

endothelial cells in the inner layer of the periosteum (Figure 2, M and N). To measure the contribution of Nestin$^+$ cells to periosteal bone growth, we quantified the percentage of periosteal osteoblasts/osteocytes derived from Nestin$^+$ lineage cells at 2 weeks, 1 month, and 2 months after tamoxifen injection in *Nestin-creERT2 R26R-EYFP* mice. Coimmunostaining of YFP with Osx, osteocalcin (Ocn), or sclerostin (Sost) showed that periosteal Nestin$^+$ cells continuously give rise to periosteal osteoblasts and osteocytes (Supplemental Figure 3, A–C). Specifically, Nestin$^+$ cells give rise to approximately 43% of periosteal Osx$^+$ and 41% of Ocn$^+$ osteoblasts after 1 month of lineage tracing, and the percentages increased to 56% and 49%, respectively, after 2 months. Moreover, approximately 8.5% of periosteal osteocytes were derived from Nestin$^+$ lineage cells (Supplemental Figure 3, A–C), which indicates the essential role of periosteal Nestin$^+$ cells during periosteal bone growth. Next, we performed coimmunostaining of Nestin with GFP in 1-month-old Nestin-GFP mice or with YFP in 1-month-old *Nestin-creERT2 R26R-EYFP* mice 48 hours after tamoxifen injection (Supplemental Figure 3, D and E). Approximately 86% of Nestin-GFP$^+$ cells and 89% of YFP$^+$ cells closely corresponded to the distribution of Nestin$^+$ cells in periosteum (Supplemental Figure 3F). Taken together, these results indicated that subsets of Nestin$^+$ and LepR$^+$ PDCs may possess stem cell characteristics and that Nestin$^+$ PDCs contribute mainly in periosteal bone formation in young mice, whereas LepR$^+$ PDCs do so in adult mice.

Macrophage-lineage cell deficiency impairs cortical bone formation and periosteum homeostasis. CSF-1–deficient (*Csf1*$^{-/-}$) mice showed markedly impaired cortical bone growth and deficiency of TRAP$^+$ cells because CSF-1 is essential for the survival of macrophage-lineage cells (47). Immunostaining of the periosteum of 1-month-old *Csf1*$^{-/-}$ mice further showed that periosteal Nestin$^+$ cells, LepR$^+$ cells, periostin expression, Osx$^+$ osteoprogenitors, and CD31^{hi}Emcn^{hi} vessels were largely missing, with a deficiency of TRAP$^+$ cells relative to their control littermates (Figure 3, A–F, and Supplemental Figure 4, A and B). Moreover, *Csf1*$^{-/-}$ mice showed markedly less thickness and cellularity of the inner layer of periosteum (Supplemental Figure 4, C and D). These results indicate that macrophage-lineage cells are essential for the maintenance of the periosteum.

Macrophage-lineage TRAP$^+$ cell deficiency impairs the recruitment of PDCs for cortical bone formation. To investigate the mechanism that modulates PDCs for periosteal cortical bone formation, we genetically ablated TRAP$^+$ cells by crossing *Trap-cre* mice with *iDTR* mice to generate *Trap-cre iDTR* mice. *Trap-cre iDTR* mice were injected with diphtheria toxin from P10 and analyzed at P30 (Figure 4A). TRAP staining confirmed that there were no TRAP$^+$ cells on the periosteal bone surface in *Trap-cre iDTR* mice (Figure 4, B and E). A high volume of unmineralized trabecular bone was formed in *Trap-cre iDTR* mice relative to their control littermates due to a deficiency of TRAP$^+$ osteoclasts (Figure 4C; Supplemental Figure 5, A–C). However, the microarchitecture, mineral apposition rate (MAR), and bone formation rate (BFR) of periosteal cortical bone in *Trap-cre iDTR* mice were significantly decreased (Supplemental Figure 5, A–C). Compared with *Csf1*$^{-/-}$ mice, the numbers (Figure 4, D, F, and G) and proliferation (Figure 4, H and I) of periosteal Nestin$^+$ and LepR$^+$ cells were not significantly different in *Trap-cre iDTR* mice. However, the migration ability of Nestin$^+$ cells to the periosteal bone surface was significantly impaired (Figure 4F), indicating that TRAP$^+$ cells regulate the migration of PDCs to the periosteal osteogenic surface, whereas PDCs are maintained by other macrophage-lineage cells rather than TRAP$^+$

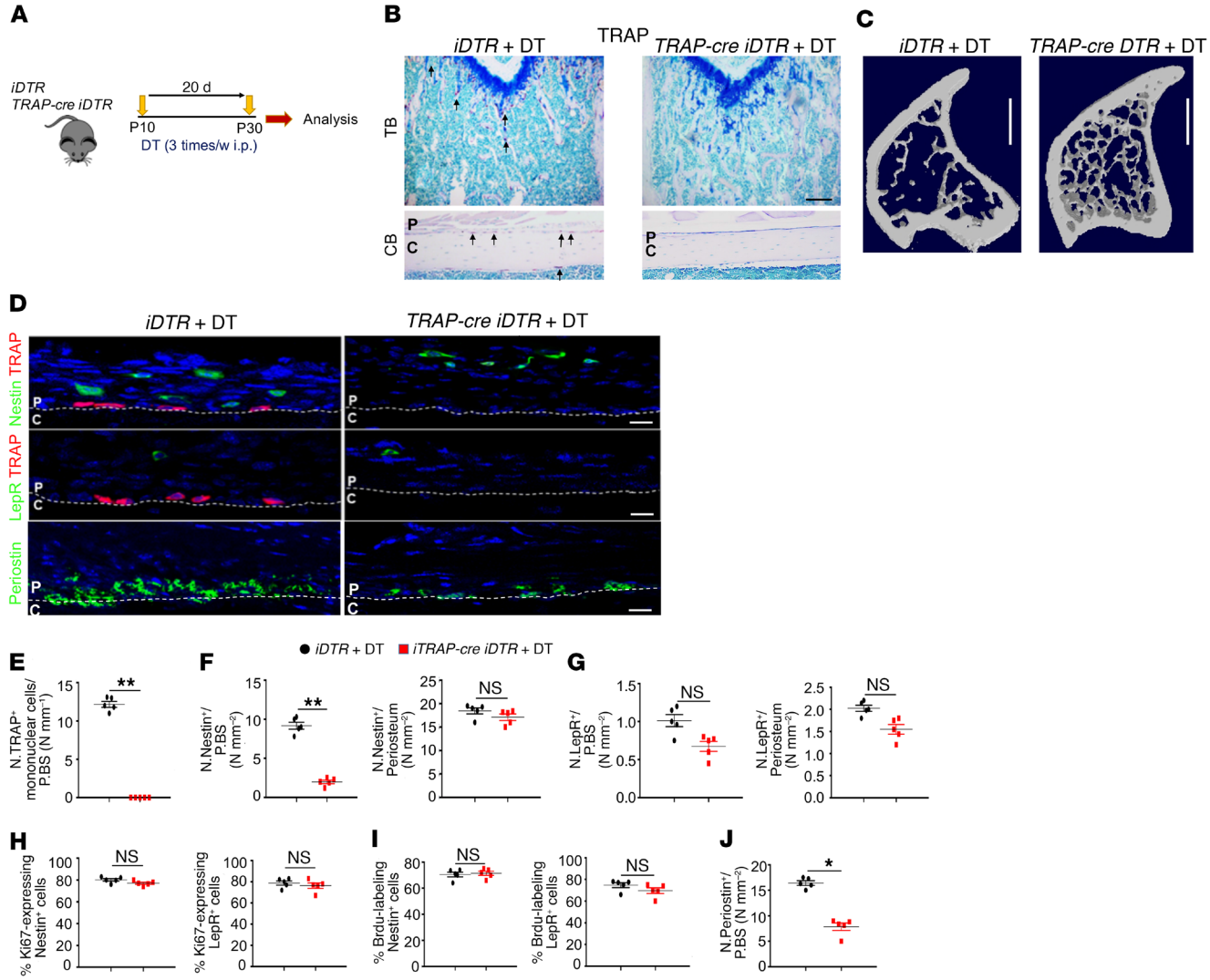

Figure 4. Ablation of TRAP⁺ cells impairs recruitment of PDCs for periosteal bone formation. (**A**) Diphtheria toxin treatment in iDTR and Trap-cre iDTR mice. (**B**) Representative TRAP staining images of coronal trabecular bone (TB) and cortical bone sections. Black arrows indicate TRAP⁺ cells. Scale bars: 300 μm (n = 5 mice/group). (**C**) Representative microcomputed tomography (μCT) images. Scale bars: 1 mm (n = 5 mice/group). (**D**–**G**) Representative images of coronal tibia diaphyseal periosteum sections stained for TRAP and Nestin (**D**, top), TRAP and LepR (**D**, middle), periostin (**D**, bottom), and quantification of the TRAP⁺ mononuclear cells (**E**), Nestin⁺ cells (**F**), and LepR⁺ cells (**G**) in the inner layer of periosteum (no. cells/P.BS) and/or whole periosteum (no. cells/periosteum). (**H** and **I**) Percentage of Ki-67⁺ (**H**) or Brdu⁺ (**I**) cells in Nestin⁺ or LepR⁺ cells on periosteum. (**J**) Quantification of periostin⁺ cells in the inner layer of periosteum (no. cells/P.BS). Scale bars: 20 μm (n = 5 mice/group). Dashed line in **D** indicates the line between periosteum and cortical bone. Data are presented as mean ± SEM. $^*P < 0.05$; $^{**}P < 0.01$. BM, bone marrow; C, cortical bone; NS, not significant as determined by 2-tailed Student t test; P, periosteum.

cells. Moreover, the periostin expression, Osx⁺ osteoprogenitors, and CD31^{hi}Emcn^{hi} vessel distributions in the inner layer were significantly decreased in *Trap-cre iDTR* mice compared with those of their control littermates (Figure 4J and Supplemental Figure 5, D and E). The number of periosteal LepR⁺ cells in young mice was too low to be detected for meaningful statistical analysis (Figure 4, D and G). As a result, the thickness and cellularity of the inner layer of periosteum were significantly decreased in mice with TRAP⁺ cell deficiency (Supplemental Figure 5, F and G).

To validate that TRAP⁺ cells are essential for cortical bone formation and periosteum homeostasis, we generated *Dmp1-cre Rankl$^{fl/fl}$* mice to reduce the number of periosteal TRAP⁺ cells (Supplemental Figure 6A). The cortical bone thickness and periosteum perimeter decreased significantly in 3-month-old *Dmp1-cre Rankl$^{fl/fl}$* mice relative to their control littermates (Supplemental Figure 6, B and C). Moreover, the recruitment of Nestin⁺ and LepR⁺ cells to the periosteal surface was significantly decreased (Supplemental Figure 6, D, E, H, and I). The thickness and cellularity of the inner layer of periosteum, expression of periostin, Osx⁺ osteoprogenitors, and CD31^{hi}Emcn^{hi} vessels also decreased in 3-month-old *Dmp1-cre Rankl$^{fl/fl}$* mice (Supplemental Figure 6, F, G, and J–M). Thus, periosteal TRAP⁺ cells induce recruitment of PDCs for cortical bone formation.

PDGF-BB secreted by TRAP⁺ mononuclear cells recruits Nestin⁺ and LepR⁺ PDCs to the periosteal surface. We previously showed that PDGF-BB secreted by TRAP⁺ mononuclear cells induces angiogenesis coupled with osteogenesis (4). Therefore, we generated *Trap-cre Pdgfb$^{fl/fl}$* mice to investigate whether PDGF-BB secreted by TRAP⁺ mononuclear cells recruits PDCs for periosteal

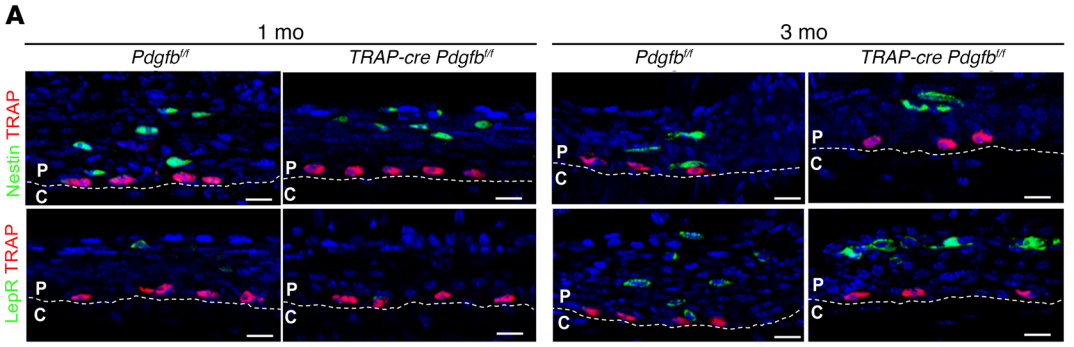
A
1 mo
3 mo
Pdgfb^f/f
TRAP-cre Pdgfb^f/f
Nestin TRAP
LepR TRAP
P
C

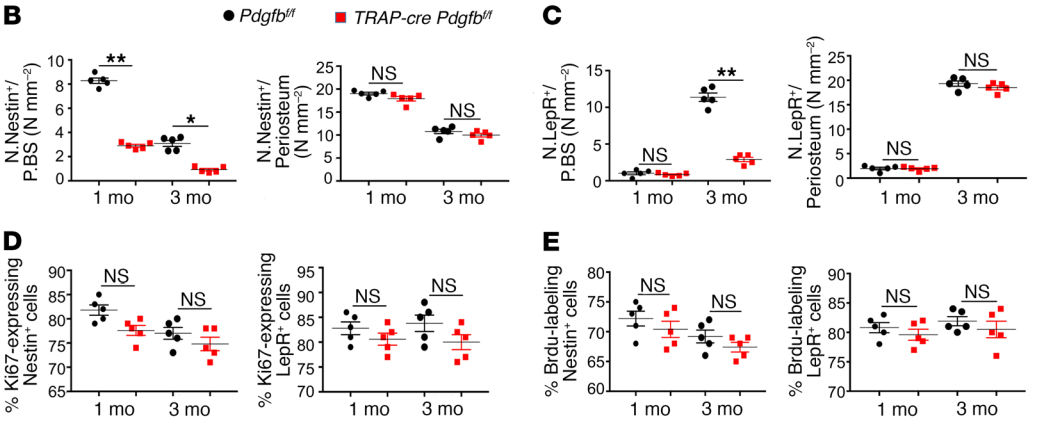
B
C
Pdgfb^f/f
TRAP-cre Pdgfb^f/f
N.Nestin+/ P.BS (N mm−2)
N.Nestin+/ Periosteum (N mm−2)
N.LepR+/ P.BS (N mm−2)
N.LepR+/ Periosteum (N mm−2)
NS
1 mo
3 mo

D
E
% Ki67-expressing Nestin+ cells
% Ki67-expressing LepR+ cells
% Brdu-labeling Nestin+ cells
% Brdu-labeling LepR+ cells
NS
1 mo
3 mo

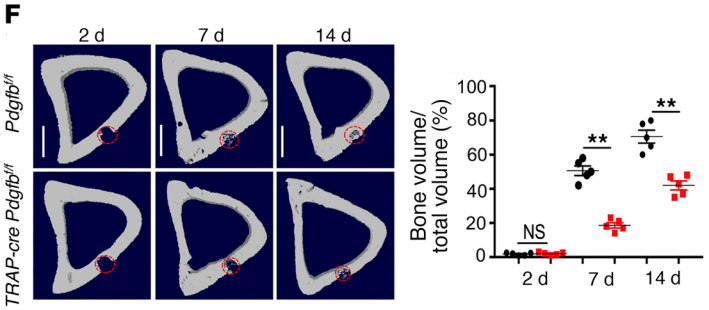
F
2 d
7 d
14 d
Pdgfb^f/f
TRAP-cre Pdgfb^f/f
Bone volume/ total volume (%)

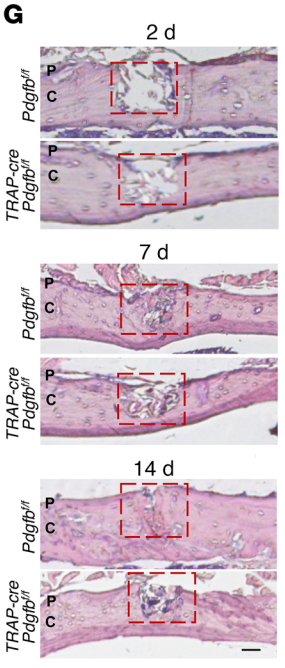
G
2 d
7 d
14 d
Pdgfb^f/f
TRAP-cre Pdgfb^f/f
P
C

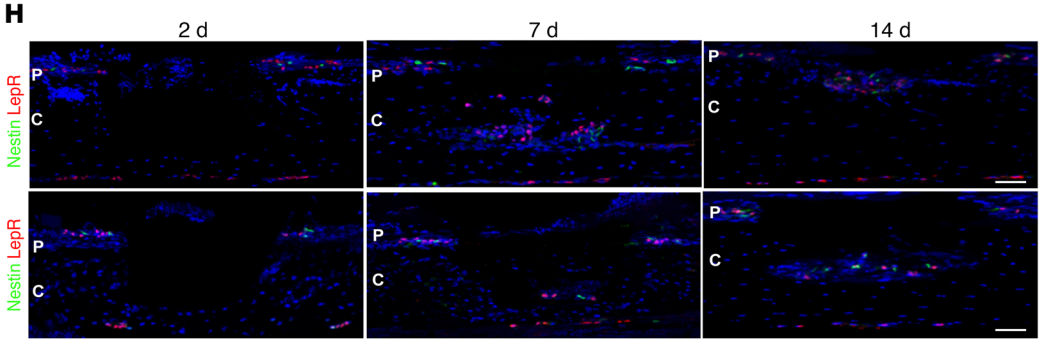
H
2 d
7 d
14 d
Nestin LepR
P
C

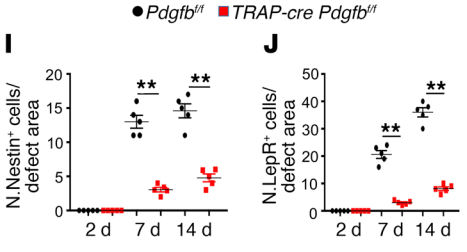
I
J
Pdgfb^f/f
TRAP-cre Pdgfb^f/f
N.Nestin+ cells/ defect area
N.LepR+ cells/ defect area
2 d
7 d
14 d

Figure 5. PDGF-BB secreted by TRAP$^+$ cells recruits PDCs to the periosteal surface for cortical bone formation. (**A**) Representative images of coronal tibia diaphyseal periosteum sections from *Trap-cre Pdgfb$^{fl/fl}$* mice and *Pdgfb$^{fl/fl}$* mice stained for TRAP and Nestin (top) and TRAP and LepR (bottom). (**B** and **C**) Quantification of Nestin$^+$ cells (**B**) and LepR$^+$ cells (**C**) in the inner layer of periosteum (no. cells/P.BS) and/or whole periosteum (no. cells/periosteum). Scale bars: 20 μm (n = 5 mice/group). (**D** and **E**) Percentage of Ki-67$^+$ (**D**) or Brdu$^+$ (**E**) cells in Nestin$^+$ or LepR$^+$ cells on periosteum (n = 5 mice/group). (**F**) Tibiae 14 days after cortical bone defect surgery. Representative μCT images of tibial cortex and quantification of the newly formed bone volume (BV/TV). Scale bars: 1 mm (n = 5 mice/group). (**G**) H&E staining of defect site sections. Red boxes indicate the defect sites. Scale bars: 200 μm (n = 5 mice/group). (**H**–**J**). Representative images of defect site sections stained for Nestin and LepR. Quantification of Nestin$^+$ cells (**I**) and LepR$^+$ cells (**J**) in the defect sites. Scale bars: 100 μm (n = 5 mice/group). Dashed lines indicate the limit between periosteum and cortical bone. Data are presented as mean ± SEM. *P < 0.05; **P < 0.01. C, cortical bone; P, periosteum; NS, not significant as determined by 2-tailed Student t test.

bone formation. The recruitment of Nestin$^+$ and LepR$^+$ cells to the periosteal surface was significantly decreased (Figure 5, A–C), whereas the total numbers (Figure 5, B and C) and proliferation (Figure 5, D and E) of these cells were not significantly changed. As a result, the microarchitecture, MAR, and BFR of periosteal cortical bone, as well as of trabecular bone, were significantly decreased in *Trap-cre Pdgfb$^{fl/fl}$* mice relative to their WT littermates at different ages (Supplemental Figure 7, A–D). Importantly, the number of Osx$^+$ osteoprogenitors and CD31^{hi}Emcn^{hi} vessels, as well as the thickness and cellularity of the inner layer, were all significantly decreased in *Trap-cre Pdgfb$^{fl/fl}$* mice relative to their WT littermates (Supplemental Figure 7, E–G), indicating the essential role of TRAP$^+$ mononuclear cells in PDC-initiated cortical bone formation and periosteum homeostasis. To determine the role of macrophage-lineage TRAP$^+$ cells in cortical bone regeneration, we established a cortical bone defect model using 3-month-old *Trap-cre Pdgfb$^{fl/fl}$* mice in which a hole was drilled in periosteal bone without penetrating the endosteal bone surface to avoid involvement of stem/progenitor cells from bone marrow and endosteum during periosteal bone regeneration. On day 14, the cortical gaps were almost completely bridged in *Pdgfb$^{fl/fl}$* mice, whereas those of *Trap-cre Pdgfb$^{fl/fl}$* mice were significantly impaired (Figure 5, F and G). Coimmunostaining showed that periosteal Nestin$^+$ and LepR$^+$ cells were recruited to the regeneration area in *Pdgfb$^{fl/fl}$* mice, whereas the recruitment of these cells was significantly decreased in *Trap-cre Pdgfb$^{fl/fl}$* mice (Figure 5, H–J). Thus, PDGF-BB secreted by macrophage-lineage TRAP$^+$ cells is essential for PDC recruitment and periosteal cortical bone regeneration.

Deletion of cathepsin K (*Ctsk*) increases TRAP$^+$ mononuclear cells and PDGF-BB secretion (4, 48). As expected, the migration of Nestin$^+$ cells to the periosteal surface increased significantly (Supplemental Figure 8, A and B) without a change in the total number (Supplemental Figure 8B, right panel) or proliferation (Supplemental Figure 8, D and E) of Nestin$^+$ cells. Notably, the number of periosteal LepR$^+$ cells in young mice was too low to statistically quantify for cell migration (Supplemental Figure 8C). Moreover, injection of CTSK inhibitor (L-235) significantly increased PDGF-BB secretion by TRAP$^+$ cells in *Nestin-creERT2 R26R-EYFP* mice. Coimmunostaining of YFP with Osx, Ocn, or Sost showed that L-235 significantly increased the percentages of osteoblasts and osteocytes derived from Nestin$^+$ lineage cells compared with vehicle control (Supplemental Figure 8F). As a result, periosteal bone thickness, the periosteum perimeter, and trabecular bone volume and thickness were significantly increased in *Ctsk$^{-/-}$* mice (Supplemental Figure 8G). Osx$^+$ osteoprogenitors and CD31^{hi}Emcn^{hi} vessels, in addition to the cellularity of the inner layer of periosteum, were significantly increased, whereas the thickness of the inner layer of periosteum was not significantly increased (Supplemental Figure 8, H–K), indicating that the periosteum thickness was maintained as in the physiological condition. These results show that PDGF-BB secreted by TRAP$^+$ mononuclear cells is essential for the recruitment of Nestin$^+$ and LepR$^+$ PDCs to the periosteal bone surface for bone formation and periosteum homeostasis.

Transcriptional expression of periostin by PDGF-BB generates an osteogenic microenvironment at the periosteal surface layer. The osteogenic microenvironment of the periosteum is essential for periosteal bone formation (49). We then examined whether PDGF-BB secreted by TRAP$^+$ mononuclear cells regulates the periosteal osteogenic microenvironment. Conditional ablation of PDGF-BB in macrophage-lineage TRAP$^+$ cells significantly reduced expression of periostin in periosteum, and an increase of PDGF-BB in *Ctsk$^{-/-}$* mice significantly upregulated periostin expression (Figure 6, A and B), suggesting that PDGF-BB induces the periosteal osteogenic microenvironment on the periosteal surface by modulating periostin expression. Previous studies showed that periostin is expressed primarily in osteoblastic cells and is a novel marker for intramembranous ossification (50–52). To examine the molecular mechanism of PDGF-BB–induced periostin expression, we sorted Nestin$^+$PDGFR-α$^+$ PDCs by FACS. Western blot and RT-PCR showed almost no detectable periostin mRNA and protein expression in PDCs. However, periostin was expressed primarily in PDC-induced osteoblasts, and PDGF-BB further promoted periostin expression in a time- and dose-dependent manner (Figure 6, C–E). We further elucidated the signaling mechanism of PDGF-BB–induced periostin upregulation. Western blot analysis showed that PDGF-BB induced the phosphorylation of PDGFR-β, phosphoinositide 3-kinase (PI3K), AKT, and cAMP-response element binding protein (CREB) 10 minutes after treatment and reached a peak at 30 minutes (Figure 6F), which was further confirmed by immunostaining (Figure 6G). Moreover, independent inhibition of PDGFR-β, PI3K, AKT, and CREB was sufficient to block the upregulation of periostin (Figure 6H), indicating that PDGF-BB induces periostin expression via the PDGFR-β/PI3K/AKT/CREB signaling pathway. To test whether PDGF-BB transcriptionally activates periostin expression, we analyzed potential binding of phosphorylation of CREB (pCREB) to periostin promoter in ChIP assays. PDGF-BB induced direct binding of pCREB to periostin promoter (Frag 2) (Figure 6, I and J), indicating transcription regulation of periostin (see complete unedited blots in the Supplemental Material). To further examine whether periostin can generate an osteogenic microenvironment, we used a modified trans-well assay by precoating periostin on the bottom surface of the upper chamber and placing the culture of PDCs in the upper chamber. Addition of PDGF-BB in the lower chamber significantly induced PDC migration, and precoating with periostin enhanced the migrated PDCs' adhesion to the bottom surface of the upper chamber, although periostin

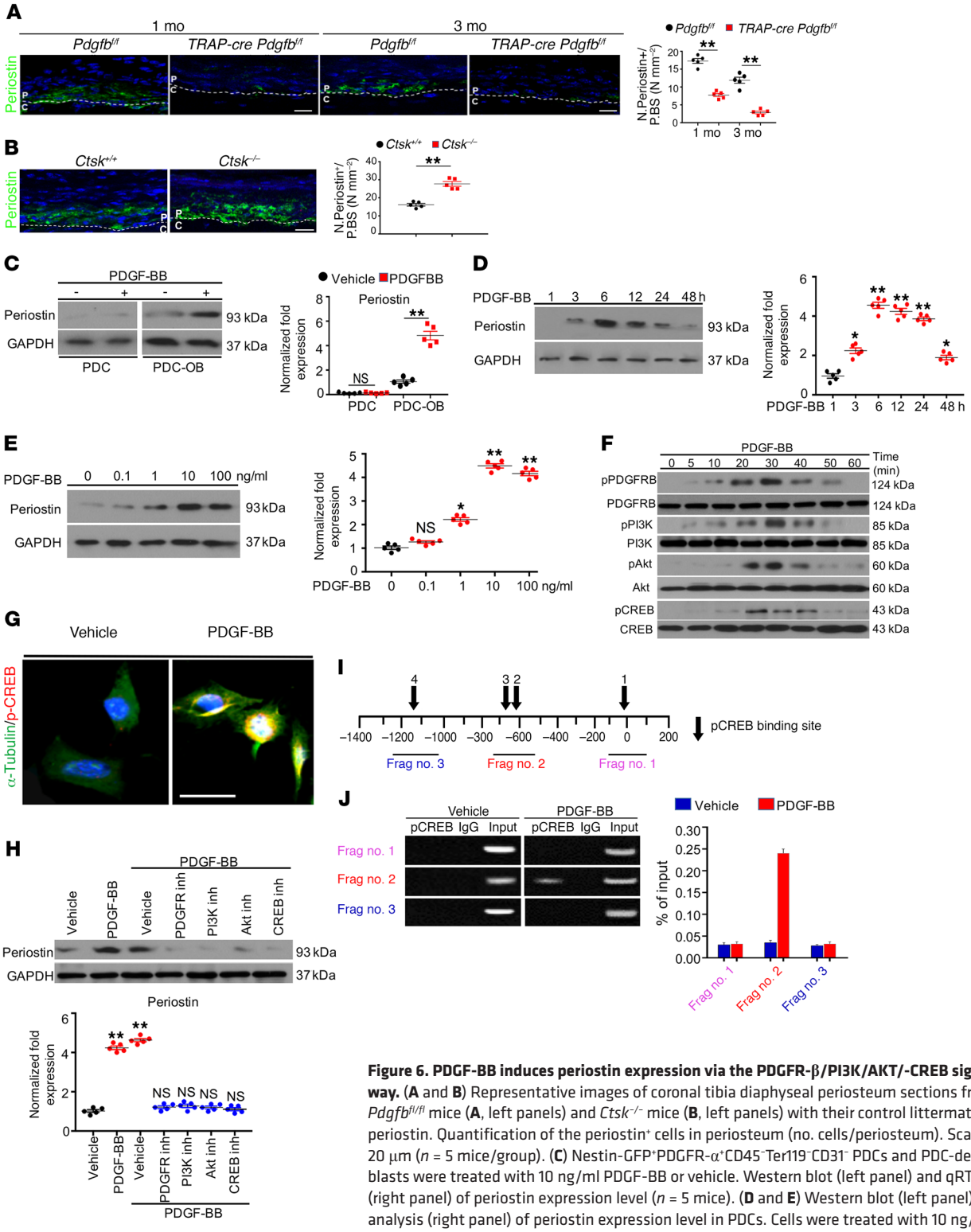

Figure 6. PDGF-BB induces periostin expression via the PDGFR-β/PI3K/AKT/-CREB signaling pathway. (**A** and **B**) Representative images of coronal tibia diaphyseal periosteum sections from *Trap-cre Pdgfb*$^{fl/fl}$ mice (**A**, left panels) and *Ctsk*$^{-/-}$ mice (**B**, left panels) with their control littermates stained for periostin. Quantification of the periostin$^+$ cells in periosteum (no. cells/periosteum). Scale bars: 20 μm (n = 5 mice/group). (**C**) Nestin-GFP$^+$PDGFR-α$^+$CD45$^-$Ter119$^-$CD31$^-$ PDCs and PDC-derived osteoblasts were treated with 10 ng/ml PDGF-BB or vehicle. Western blot (left panel) and qRT-PCR analysis (right panel) of periostin expression level (n = 5 mice). (**D** and **E**) Western blot (left panel) and qRT-PCR analysis (right panel) of periostin expression level in PDCs. Cells were treated with 10 ng/ml PDGF-BB or vehicle for the indicated times (**D**) or with the indicated doses of PDGF-BB or vehicle for 6 hours (**E**) (n = 5 mice). (**F**) Western blot analysis of the phosphorylation of PDGFR-β, PI3K, AKT, and CREB (n = 5 mice). (**G**) Representative images stained for p-CREB and α-Tubulin in PDC-derived osteoblasts. Scale bars: 10 μm (n = 5 mice). (**H**) Western blot (left panel) and qRT-PCR analysis (right panel) of periostin expression levels in PDC-derived osteoblasts. Cells were treated with 10 ng/ml PDGF-BB or vehicle in the presence or absence of various inhibitors, as indicated (n = 5 mice). (**I**) p-CREB binding sites on periostin promoter. (**J**) ChIP analysis of p-CREB on specific periostin promoter regions in the cells with PDGF-BB or vehicle treatment (n = 3 mice). Data are presented as mean ± SEM. *P < 0.05; **P < 0.01; NS, not significant as determined by 2-tailed Student t test.

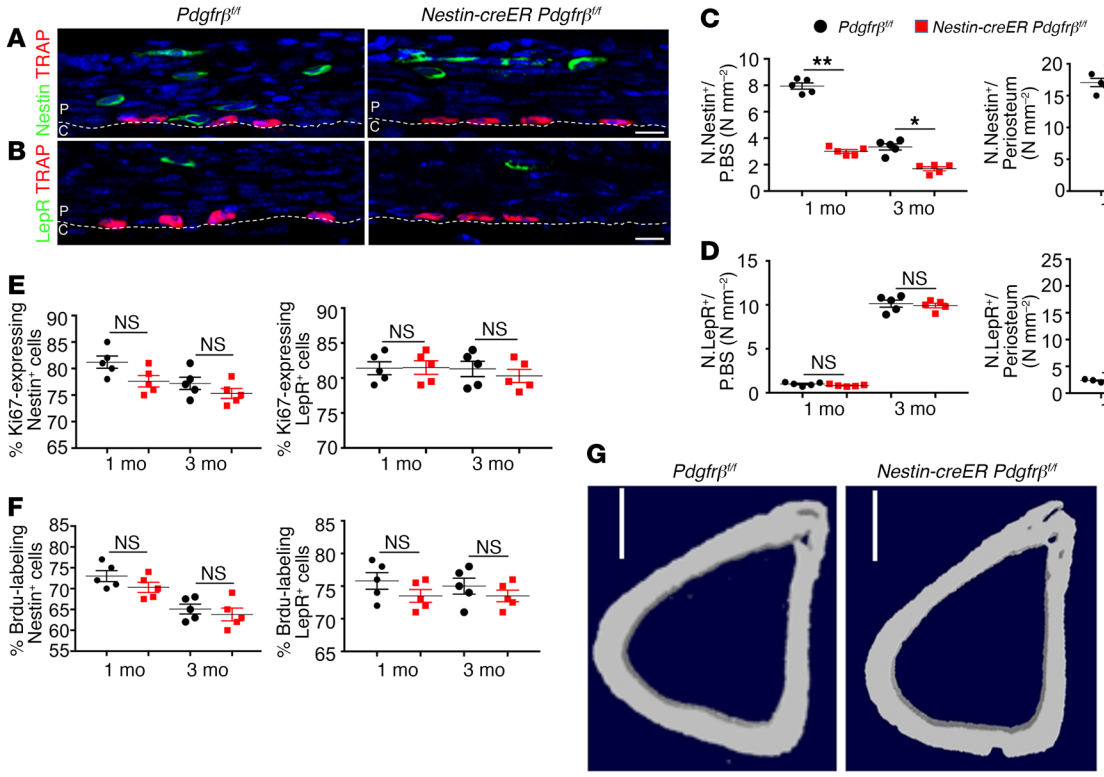

Figure 7. Knockout of *Pdgfr-β* in Nestin⁺ cells impairs recruitment of PDCs and periosteal bone formation in young mice. (**A** and **B**) Representative images of coronal tibia diaphyseal periosteum sections from *Nestin-creERT2 Pdgfr-β*$^{fl/fl}$ mice and their control littermates (*Pdgfr-β*$^{fl/fl}$) stained for TRAP and Nestin (**A**) and TRAP and LepR (**B**). (**C** and **D**) Quantification of Nestin⁺ cells (**C**) and LepR⁺ cells (**D**) in the inner layer of periosteum (no. cells/P.BS) and/or whole periosteum (no. cells/periosteum). Scale bars: 20 μm (n = 5 mice/group). (**E** and **F**) Percentage of Ki-67⁺ (**E**) or Brdu⁺ (**F**) cells in Nestin⁺ or LepR⁺ cells on periosteum (n = 5 mice/group). (**G**) Representative μCT images. Dashed line indicates the line between periosteum and cortical bone. Data are presented as mean ± SEM. *P < 0.05; **P < 0.01. Scale bars: 1 mm (n = 5 mice/group). 1 M, 1-month-old; 3 M, 3-month-old; C, cortical bone; P, periosteum; NS, not significant as determined by 2-tailed Student t test.

itself did not promote PDC migration (Supplemental Figure 9, A and B). Periostin promoted osteogenesis of PDCs (10 μg/ml) in Alizarin red staining (Supplemental Figure 9, C and D) and adhesion (Supplemental Figure 9, E and F) of PDCs (1 μg/ml) in a dose-dependent manner. Thus, although PDGF-BB recruits PDCs to the periosteal bone surface, it also induces periostin secretion to generate a periosteal osteogenic microenvironment for differentiation and adhesion of PDCs.

Conditional knockout of Pdgfr-β in Nestin⁺ or LepR⁺ cells impairs their recruitment for periosteal bone formation. To validate whether Nestin⁺ or LepR⁺ PDCs are recruited by PDGF-BB for periosteal bone formation and regeneration, we generated *Nestin-creERT2 Pdgfr-β*$^{fl/fl}$ and *LepR-cre Pdgfr-β*$^{fl/fl}$ mice. The recruitment of Nestin⁺ cells to the periosteal bone surface was significantly impaired in both 1- and 3-month-old *Nestin-creERT2 Pdgfr-β*$^{fl/fl}$ mice. First, we injected 2-week-old *Nestin-creERT2 Pdgfr-β*$^{fl/fl}$ mice with tamoxifen to knock out *Pdgfr-β* and investigated their phenotype at 1 month old. Second, we injected 2-month-old *Nestin-creERT2 Pdgfr-β*$^{fl/fl}$ mice with tamoxifen and investigated their phenotype at 3 months old. Recruitment of Nestin⁺ cells to the periosteal bone surface was significantly impaired compared with control littermates in both 1- and 3-month-old *Nestin-creERT2 Pdgfr-β*$^{fl/fl}$ mice (Figure 7A), whereas the total number (Figure 7C) and proliferation (Figure 7, E and F) of periosteal Nestin⁺ cells were not significantly decreased. Knockout of *Pdgfr-β* in Nestin⁺ cells did not significantly affect the number and migration of periosteal LepR⁺ cells (Figure 7, B and D). Interestingly, the microarchitecture, MAR, and BFR of periosteal cortical bone were impaired only in 1- and not 3-month-old *Nestin-creERT2 Pdgfr-β*$^{fl/fl}$ mice (Figure 7G and Supplemental Figure 10, A and B), indicating that Nestin⁺ PDCs contribute to periosteal bone formation during youth but not in adulthood. Importantly, periostin expression and Osx⁺ osteoprogenitors, in addition to the inner layer thickness, were decreased significantly in 1- but not 3-month-old *Nestin-creERT2 Pdgfr-β*$^{fl/fl}$ mice (Supplemental Figure 10, C, D, G, and I). Notably, CD31^{hi}Emcn^{hi} vessels and inner layer cellularity were significantly decreased in both 1- and 3-month-old *Nestin-creERT2 Pdgfr-β*$^{fl/fl}$ mice compared with their control littermates (Supplemental Figure 10, H and I, right panel). These results indicate the essential role of Nestin⁺ PDCs in periosteal bone formation coupled with vessel formation during postnatal bone development.

In contrast, knockout of *Pdgfr-β* in LepR⁺ cells showed that LepR⁺ PDCs contribute to periosteal bone formation mainly in adult mice. Specifically, the recruitment of LepR⁺ cells to the periosteal surface was significantly impaired (Figure 8, A, B, and D) in 3-month-old mice relative to control littermates, whereas the total number (Figure 8D) and proliferation were not significantly decreased (Figure 8, E and F). Knockout of *Pdgfr-β* in LepR⁺ cells

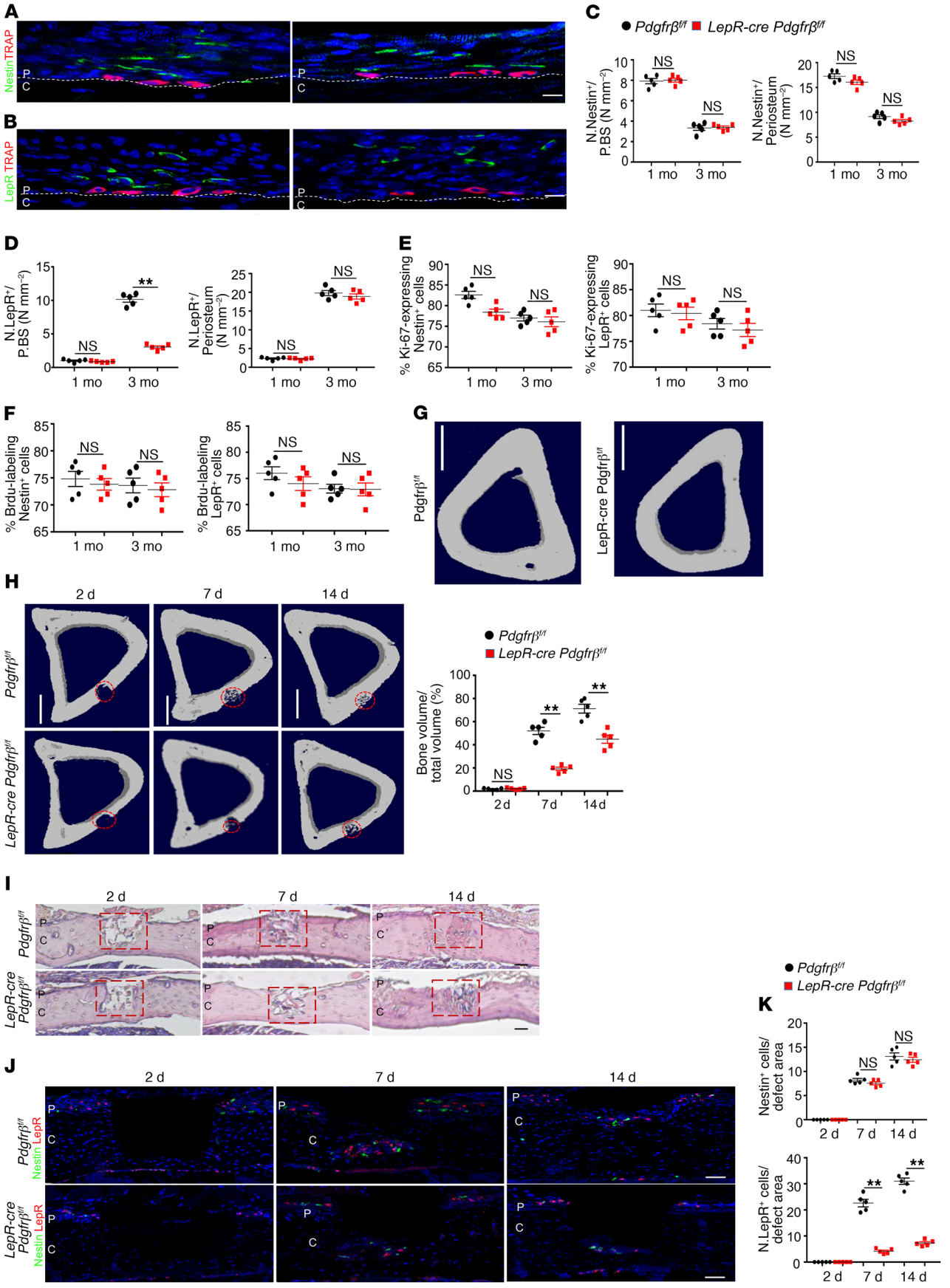
A
B
C
D
E
F
G
H
I
J
K
Nestin TRAP
LepR TRAP
P
C
Pdgfrβ^f/f
LepR-cre Pdgfrβ^f/f
N.Nestin+/ P.BS (N mm−2)
N.Nestin+/ Periosteum (N mm−2)
N.LepR+/ P.BS (N mm−2)
N.LepR+/ Periosteum (N mm−2)
% Ki-67-expressing Nestin+ cells
% Ki-67-expressing LepR+ cells
% Brdu-labeling Nestin+ cells
% Brdu-labeling LepR+ cells
Bone volume/ total volume (%)
Nestin+ cells/ defect area
N.LepR+ cells/ defect area
NS
1 mo
3 mo
2 d
7 d
14 d
Nestin LepR

Figure 8. Knockout of *Pdgfr-β* in LepR$^+$ cells impairs recruitment of PDCs and periosteal bone formation in adult mice. (**A** and **B**) Representative images of coronal tibia diaphyseal periosteum sections from *LepR-cre Pdgfr-β$^{fl/fl}$* mice and *Pdgfr-β$^{fl/fl}$* mice stained for TRAP and Nestin (**A**) and TRAP and LepR (**B**). (**C** and **D**) Quantification of Nestin$^+$ cells (**C**) and LepR$^+$ cells (**D**) in the inner layer of periosteum (no. cells/P.BS) and/or whole periosteum (no. cells/periosteum). Scale bars: 20 μm (*n* = 5 mice/group). (**E** and **F**) Percentage of Ki-67$^+$ (**E**) or Brdu$^+$ (**F**) cells in Nestin$^+$ or LepR$^+$ cells on periosteum (*n* = 5 mice/group). (**G**) Representative μCT images. Scale bars: 1 mm (*n* = 5 mice/group). 1 M, 1-month-old; 3 M, 3-month-old. (**H**) Tibiae 14 days after cortical bone defect surgery. Representative μCT images of tibial cortex and quantification of newly formed bone volume (BV/TV). Scale bars: 1 mm (*n* = 5 mice/group). (**I**) H&E staining of defect site sections. Red boxes indicate the defect sites. Scale bars: 200 μm (*n* = 5 mice/group). (**J** and **K**) Representative images of defect site sections stained for Nestin and LepR. Quantification of Nestin$^+$ cells (**K**, left panel) and LepR$^+$ cells (**K**, right panel) in the defect sites. Scale bars: 100 μm (*n* = 5 mice/group). Dashed lines indicate the limit between periosteum and cortical bone. Data are presented as mean ± SEM. $^*P < 0.05$; $^{**}P < 0.01$. C, cortical bone; P, periosteum; NS, not significant as determined by 2-tailed Student *t* test.

did not significantly affect the migration and proliferation of periosteal Nestin$^+$ cells, the number of CD31^{hi}Emcn^{hi} vessels, or the inner layer thickness of the periosteum (Figure 8, C, E, and F; Supplemental Figure 11, E, F, H, and I). Nevertheless, periostin expression, Osx$^+$ osteoprogenitors, and the inner layer cellularity of periosteum were significantly decreased in 3-month-old *LepR-cre Pdgfr-β$^{fl/fl}$* mice (Supplemental Figure 11, C, D, F, and I). As a result, the microarchitecture, MAR, and BFR of periosteal cortical bone were significantly decreased in 3- but not 1-month-old *LepR-cre Pdgfr-β$^{fl/fl}$* mice (Figure 8G; Supplemental Figure 11, A–C). To further determine whether the recruitment of LepR$^+$ PDCs by macrophage-lineage TRAP$^+$ cells is essential during cortical bone regeneration, we established a cortical bone defect model, as described previously, using 3-month-old *LepR-cre-cre Pdgfr-β$^{fl/fl}$* mice and found the cortical gaps were almost completely bridged in *Pdgfr-β$^{fl/fl}$* mice in 14 days, whereas those of *LepR-cre Pdgfr-β$^{fl/fl}$* mice were significantly impaired (Figure 8, H and I). Coimmunostaining showed that the recruitment of LepR$^+$ cells to the defect region were significantly decreased in *LepR-cre Pdgfr-β$^{fl/fl}$* mice (Figure 8, J and K). Thus, the recruitment of PDCs by macrophage-lineage TRAP$^+$ cells is essential for periosteal cortical bone regeneration. These results show that periosteal Nestin$^+$ and LepR$^+$ PDCs are modulated by macrophage-lineage TRAP$^+$ cells to play different roles in periosteal bone formation and regeneration (Supplemental Figure 12, A and B).

Discussion

Periosteum provides an essential environment for cortical bone growth, bone modeling, and fracture healing (29, 30). Although great effort has been made to investigate the mechanism of periosteal bone formation (1, 2, 13), we still know little about the osteogenic nature of the periosteum and how PDCs are maintained to regulate cortical bone formation and bone regeneration. In this study, we found a mechanism in which periosteal macrophage-lineage cells regulate the periosteum osteogenic microenvironment for cortical bone formation and regeneration. Moreover, TRAP$^+$ cells induce transcriptional expression of periostin and recruit PDCs to the periosteal surface. The recruited PDCs undergo osteoblast differentiation, coupled with type H vessel formation (Supplemental Figure 12B). Also, subsets of periosteal Nestin$^+$ cells and LepR$^+$ cells were identified as the stem/progenitor cells residing in the outer layer of periosteum. Knockout of *Csf1* eliminates macrophage-lineage cells (47, 53, 54), and consequently, their cellular activity and matrix proteins were significantly reduced in the periosteum. Therefore, periosteal macrophage-lineage cells are essential in the maintenance of PDCs, and macrophage sublineage TRAP$^+$ mononuclear cells recruit PDCs to the periosteal bone surface for osteogenesis coupled with type H vessel formation.

Macrophages are present in most tissues for homeostasis and regeneration. Resident tissue macrophages of bone in the myeloid lineage can be distinct from osteoclasts. It is likely that different macrophage subtypes play different roles in bone formation, bone regeneration, and fracture healing. We investigated periosteal TRAP$^+$ cells primarily where the muscles overlie the periosteum, not at sites of muscle-tendon insertions or the sites where muscles arise. Specific ablation of macrophage-lineage TRAP$^+$ cells or conditional knockout of PDGF-BB in TRAP$^+$ cells significantly reduced Nestin$^+$ cells and LepR$^+$ cells on the periosteal surface, while the proliferation of these cells remained unchanged. Interestingly, 3-month-old *Dmp1-Cre Rankl$^{fl/fl}$* mice developed impaired cortical bone formation, while 1-month-old transgenic mice did not develop significant impaired phenotypes. This observation was consistent with the number of TRAP$^+$ cells in mice of different ages, which further shows the important role of TRAP$^+$ cells in periosteal bone formation. There is a limitation in this animal model for TRAP$^+$ cell investigation for young mice, as the number of TRAP$^+$ cells is normal in 1-month-old *Dmp1-cre Rankl$^{fl/fl}$* mice. This is likely because osteocytes are not the primary source of Rankl during bone development.

Although remodeling of trabecular bone occurs in the bone marrow microenvironment, growth and modeling of cortical bone take place in the periosteum, which covers the outer surface of cortical bone. In young bones, the periosteum is thick with rich vascular supply, but later in life, it is thinner with less vascularity. Bones that lose the periosteum secondary to injury or disease usually scale or die. During growth or modeling, periosteal cortical bone formation, in coordination with endocortical bone resorption, leads to the expansion in diameter of the long bones. Periosteal expansion of cortical bone can substantially increase bone strength, independent of bone mass density. The periosteum provides a supportive microenvironment with vasculature, nerves, PDCs, and osteoprogenitors, which resembles a unique bone marrow for the growth and modeling of cortical bone. A recent study showed that PSCs are present in the long bones and calvarium and display clonal multipotency and self-renewal ability distinct from those of other skeletal stem cells and mature mesenchymal cells (12). Duchamp de Lageneste et al. also showed that the periosteum contains skeletal stem cells with high bone regenerative potential relative to bone marrow stromal cells/skeletal stem cells (14). Colnot et al. investigated periosteal Prx1$^+$ cells and showed that periostin is required to maintain the pool of periosteum skeleton stem cells and that lack of periostin impairs periosteum function and bone healing (14). We found that macrophage/monocytes differentiate into periosteal TRAP$^+$ mononuclear cells during bone growth and secrete PDGF-BB, which transcriptionally induces expression of periostin to generate an osteogenic

microenvironment in the periosteal surface layer. Conditional ablation of PDGF-BB in macrophage-lineage TRAP$^+$ cells significantly reduced periostin expression in the periosteum (Figure 6A). Mechanistically, PDGF-BB upregulated periostin expression via inducing the phosphorylation of PDGFR-β, PI3K, AKT, and CREB. CREB is essential for enhanced osteogenic formation, which is modulated by PI3K/AKT signaling (55, 56), but the downstream target of CREB in PDCs has not been well characterized. We showed that PDGF-BB could induce direct binding of pCREB to periostin promoter in ChIP assay. This finding reveals the mechanism by which periostin expression induced by TRAP$^+$ mononuclear cells maintains the periosteum microenvironment and regulates differentiation of PDCs for periosteum homeostasis and osteogenesis.

We sought to investigate the molecular and cellular mechanisms of periostin in regulating periosteal bone formation in adult mice. Because there are many types of cells in the periosteum, we chose to use PDCs, which cover a broad spectrum of cells from periosteum stem cells to their progenitors at different stages of differentiation. Periostin provides an osteogenic microenvironment and likely regulates osteoprogenitors, in addition to maintaining periosteum stem cells. Subsets of periosteal Nestin$^+$ cells and LepR$^+$ cells of PDCs were investigated. Nestin-GFP$^+$ PDCs are abundant in young mice with multidifferential potency and significantly decreased in adulthood (Figures 1 and 7, and Supplemental Figures 1 and 10). In contrast, LepR$^+$ cells were abundantly localized in periosteum only in adult mice. Notably, periosteum skeleton stem cells characterized from Prx1$^+$ cells during development likely have some overlaps with Nestin-GFP$^+$ PDCs, whereas LepR$^+$ cells are primarily found in adult mice may not have much overlap with Prx1$^+$ cells. In contrast to bone marrow, periosteum does not appear to contain hematopoietic stem cells. Therefore, the unique microenvironment is exclusively responsible for maintaining PDCs and periosteal bone formation. The periosteal macrophage-lineage cells primarily regulate and maintain PDCs for the osteogenic and bone regenerative ability of periosteum. This finding, however, does not preclude the involvement of other cells, such as endothelial cells, in the regulation of PDCs.

Methods

Animals and treatment. We purchased the following mouse strains from the Jackson Laboratory: *Csf1*$^{-/-}$ (no. 000231), *B6-iDTR* (no. 007900), *Pdgfb*$^{fl/fl}$ (no. 017622), *Nestin-cre*^{ERT2} (no. 016261), *LepR-cre* (no. 008320), *Dmp1-cre* (no. 023047), *R26R-EYFP* (no. 006148), *Rankl*$^{fl/fl}$ (no. 018978), and *Pdgfr-β*$^{fl/fl}$ (no. 010977). *Nestin-GFP* mice were provided by Grigori Enikolopov at Cold Spring Harbor Laboratory (Cold Spring Harbor, New York, USA). *Trap-cre* mice were obtained from J.J. Windle (Virginia Commonwealth University, Richmond, Virginia, USA) (57). *Ctsk*$^{-/-}$ mice were obtained from the Bone Biology Group of Merck Research Laboratories. *Csf1*$^{-/-}$ offspring and their WT littermates were generated by crossing 2 heterozygote *Csf1*^{op} strains. Hemizygous *TRAP-cre* mice were crossed with *Pdgfb*$^{fl/fl}$ mice. The offspring were intercrossed to generate the following offspring: WT mice, *TRAP-cre* mice (expressing Cre recombinase driven by TRAP promoter), *Pdgfb*$^{fl/fl}$ mice (homozygous for Pdgfb^{fl} allele), and *TRAP-cre Pdgfb*$^{fl/fl}$ mice.

Trap-cre mice were crossed with *B6-iDTR* mice. The offspring were intercrossed to generate *TRAP-cre iDTR* mice and *iDTR* mice. To delete TRAP$^+$ cells, we administered diphtheria toxin (4 μg/kg^{-1}, i.p.) to *TRAP-cre iDTR* and *iDTR* mice (as a control).

Ctsk$^{-/-}$ offspring and their WT littermates were generated by crossing 2 heterozygote strains as previously described (58). We analyzed male mice at 1 month of age, except as noted in specific experiments. For L-235 studies, we treated 2-week-old *Nestin-creERT2 R26R-EYFP* mice daily with 20 mg/kg^{-1} BW L-235 (Merck) for 4 weeks. L-235 was administered i.p. in a 0.5% Methocel (wt/vol) suspension.

Nestin-creERT2 or LepR-cre mice were crossed with *Pdgfr-β*$^{fl/fl}$ mice. The offspring were intercrossed to generate *Nestin-creERT2 Pdgfr-β*$^{fl/fl}$ mice and *Pdgfr-β*$^{fl/fl}$ mice or *LepR-cre Pdgfr-β*$^{fl/fl}$ mice and *Pdgfr-β*$^{fl/fl}$ mice. To induce Cre recombinase activity, we injected mice at designated time points with tamoxifen (100 mg/kg BW). The genotypes of the mice were determined by PCR analyses of genomic DNA extracted from mouse tail snips using the following primers: *Csf1*^{op} allele forward, 5′-TGCTAACCTCGTGGTTCCTG-3′ and reverse, 5′-GTTAGCATTGGGGGTGTTGT-3′; *TRAP-cre* forward, 5′-ATATCTCACGTACTGACGGTGGG-3′ and reverse, 5′-CTGTTTCACTATCCAGGTTACGG-3′; *loxP Pdgfb* allele forward, 5′-GGGTGGGACTTTGGTGTAGAGAAG-3′ and reverse, 5′-GGAACGGATTTTGGAGGTAGTGTC-3′; *Ctsk* forward, 5′-GCCACACCCACACCCTAGAAG-3′ and reverse, 5′-ACAAGTGTACATTCCCGTACC-3′; *Nestin-cre* forward, 5′-GCG GTC TGG CAG TAA AAA CTA TC-3′ and reverse, 5′-GTG AAA CAG CAT TGC TGT CAC TT-3′; *Nestin-GFP* allele forward, 5′-GGA GCT GCA CAC AAC CCA TTG CC-3′ and reverse, 5′-GAT CAC TCT CGG CAT GGA CGA GC-3′; *LepR-cre* forward, 5′-CTT GGG TGG AGA GGC TAT TC-3′ and reverse, 5′-AGG TGA GAT GAC AGG AGA TC-3′; *loxP Pdgfr-β* allele forward, 5′-CCA GTT AGT CCA CTT ATG TTG-3′ and reverse, 5′-TAC CAG GAA GGC TTG GGA AG-3′; *Dmp1-cre* forward, 5′-CCCGCAGAACCTGAAGATG-3′ and reverse, 5′-GACCCGGCAAAACAGGTAG-3′; *loxp Rankl* allele forward, 5′-CTGGGAGCGCAGGTTAAATA-3′ and reverse, and 5′-GCCAATAATTAAAATACTGCAGGAAA-3′.

For bromodeoxyuridine (BrdU) administration, mice were given an i.p. injection of 100 mg BrdU/kg BW in Dulbecco's phosphate buffered saline (Gibco Laboratories) and were maintained on 1 mg/ml BrdU in the drinking water for 10 days before euthanasia. Amber bottles containing BrdU water were changed every 1 to 3 days.

Micro-CT analysis. We dissected femora and tibiae from mice free of soft tissue, fixed them overnight in 70% ethanol, and analyzed data by high-resolution μCT (SkyScan 1172, Bruker) (46, 59, 60). The scanner was set at a voltage of 49 kV, a current of 200 μA, and a resolution of 8.7 μm/pixel. We used image reconstruction software (NRecon, v1.6, Micro Photonics), data analysis software (CTAn, v1.9, Bruker), and 3-dimensional model visualization software (μCT-Vol, v2.0, Bruker) to analyze the parameters of diaphyseal cortical bone and proximal tibia metaphyseal trabecular bone. We obtained cross-sectional images of the tibia to perform 2-dimensional morphometric analyses of cortical bone and 3-dimensional histomorphometric analysis of trabecular bone. The trabecular bone region of interest consisted of approximately 120 slices that were drawn starting from approximately 0.1 mm distal to the growth plate, constituting 0.7 mm in length. Trabecular bone was segmented from the bone marrow and analyzed to determine the trabecular bone volume fraction (BV/TV) and trabecular thickness. The region of interest of cortical analyses consisted of approximately 60 slices covering a length of 0.24 mm at the tibial midshaft. We analyzed cortical bone to determine cortical thickness and periosteal perimeter. For the analysis of periosteal

cortical bone regeneration, we defined the volume of interest as a cylindrical area covering the initial bone defect. Bone volume (BV/TV, %) was calculated within the delimited volume of interest.

Bone defect model. Three-month-old *TRAP-cre Pdgfb$^{fl/fl}$* mice and *LepR-cre Pdgfrb$^{fl/fl}$* mice with their control littermates were anesthetized with an i.p. injection of ketamine (100 mg/kg^{-1}) and xylazine (10 mg/kg^{-1}). In addition, buprenorphine (0.05 mg/kg^{-1}) was given for perioperative analgesia to minimize pain. Tibial cortical bone defects were created without penetrating the endosteal bone surface to exclude bone marrow progenitor cells and endosteal progenitor cells involved in periosteal cortical bone regeneration. Briefly, the anteromedial surfaces of the proximal one-third of the tibia were exposed by blunt dissection of the subcutaneous tissue after skin incision. The defect was generated using a 0.7-mm-diameter needle without penetrating the endosteal bone surface (drill depth, 0.5–0.6 mm). During drilling, a 5-ml syringe of normal saline was used to continuously flush away the bone debris. The pore size was determined by Vernier caliper.

Cell sorting and flow cytometric analysis. We performed flow cytometric analysis and sorting of CD45$^-$CD31$^-$Ter119$^-$GFP$^+$PDGFR-α$^+$ periosteal progenitor cells from periosteum of *Nestin-GFP* mice and CD45$^-$ CD31$^-$ Ter119$^-$ YFP$^+$ periosteal progenitor cells from *LepR-cre R26R-EYFP* mice. We first removed bone marrow by repeated flushing of the marrow cavities with serum-free minimal essential media with alpha modifications (α-MEM). Periosteum was then scraped off after carefully removing the muscle fibers under a dissecting microscope and pooled in a Petri dish. The tissues were minced, digested for 3 hours at 37°C with type II collagenase (0.2%; Sigma-Aldrich), and passed through a 40-μm filter (Becton Dickinson) to yield single-cell suspensions. Cells (5×10^5) were then collected for flow cytometry. After the process of red blood cell lysis with commercial ammonium-chloride-potassium lysis buffer (Quality Biological), cells were then sorted according to side scatter and GFP and PDGFR-α expression or YFP expression after negative selection of CD45, CD31, and Ter119. FACS was performed using a 5-laser BD FACS and FACSDiva (BD Biosciences). Flow cytometric analyses were performed using a FACSCalibur flow cytometer, CellQuest software (BD Biosciences), and FlowJo software (Tree Star). The primary antibodies used were FITC-conjugated anti-GFP (Abcam, ab290), APC mouse anti-mouse CD45.1 (BD Biosciences, 561873), APC rat anti-mouse CD31 (BD Biosciences, 561814), APC rat anti-mouse TER119 (BD Biosciences, 561033), PE rat anti-mouse CD140A (BD Biosciences, 562776), anti–PDGFR-β biotin (eBioscience, clone APB5, 1:200), anti–LepR-biotin (R&D Systems, BAF497), PerCP-conjugated anti-CD105 (BioLegend, CA 120415), and biotin anti-mouse CD90.2 (BioLegend, 105304).

Immunocytochemistry, immunofluorescence, and histomorphometry. At the time of euthanasia, mice tibiae were dissected and fixed with intact periosteum in 10% buffered formalin for 24 hours, decalcified in 10% EDTA (pH, 7.4) (Amresco) for 2 days, and embedded in paraffin or optimal cutting temperature compound (Sakura Finetek). We processed 4-μm-thick coronal (longitudinally) oriented sections of bone, including the metaphysis and diaphysis, for TRAP staining using a staining kit (MilliporeSigma). Immunofluorescence analysis of the bone sections was performed as described previously (6, 44). Longitudinally oriented 30-μm-thick sections were cut from anterior to posterior for immunofluorescence staining. The first section was determined when the tibial tuberosity appeared and the last section was determined when cortical bone and periosteum disappeared. We chose the medial sections as the selected plane, which enabled us to investigate the complete cortical bone and periosteum of the tibia. The slides were numbered to indicate the depth of the sections, and slides with comparable numbers from different groups were chosen to ensure that similar anatomical levels were compared. The diaphysis was defined to be a 1-mm section centered at the midpoint between the growth plate and the end of the tibia. We incubated the sections with primary antibodies to Nestin (Abcam, ab6142, 1:100 or Aves Labs, NES, 1:100), LepR (R&D Systems, BAF497, 1:200), TRAP (Abcam, ab185716, 1:200 or ab212723, 1:100), Osterix (Abcam, ab22552, 1:200), Sostdc1 (Abcam, ab99340, 1:100), Brdu (Abcam, ab6326, 1:250), Endomucin (Santa Cruz Biotechnology, sc-65495, 1:100), pecam1 (CD31) (Abcam, ab119341, 1:100), periostin (Abcam, ab14041, 1:100), Ki-67 (Novus Biologicals, NB500-170, 1:100), and GFP (Rockland Immunochemicals, 600-101-215M,1:500 or Abcam, ab290, 1:200), followed by incubation with FITC, or Cy3-conjugated secondary antibodies (Jackson ImmunoResearch Laboratories) or goat anti-rabbit, goat anti-chicken, goat anti-mouse, donkey anti-chicken, or donkey anti-goat (Jackson ImmunoResearch Laboratories) secondary antibodies. Nuclei were counterstained with DAPI (Sigma-Aldrich). The inner layer of periosteum was defined as a stack of 3 to 6 cells on the periosteal surface, depending on the ages of mice. We quantified the number of cells in the diaphyseal periosteum with the following parameters: (a) the number of cells per periosteal cortical bone surface (no. cells/P.BS with the unit of N × mm^{-1}), (b) the number of cells per inner layer of periosteum area (no. cells/P.BS with the unit of N × mm^{-2}), or (c) the number of cells per the whole diaphyseal periosteum area (no. cells/periosteum with the unit of N × mm^{-2}). We used an LSM 780 FCS confocal microscope (Zeiss) or a BX51 microscope (Olympus) for imaging samples.

To examine dynamic bone formation, we subcutaneously injected 0.1% calcein (Sigma-Aldrich, 10 mg/kg BW) in phosphate-buffered saline into the mice 10 and 3 days before euthanasia. We observed calcein double-labeling in undecalcified bone slices under a fluorescence microscope to quantify mineralizing surfaces of periosteal, endosteal, and trabecular bone (MAR, μ/d; BFR/bone surface, μm^3/μm^2/d).

ChIP and antibodies. ChIP was performed according to instructions from the Simple Chip Enzymatic Chromatin IP Kit (no. 9003, Cell Signaling Technology) with ChIP-grade antibodies to pCREB (no. 9198, Cell Signaling Technology). Briefly, we added cells with formaldehyde to cross-link proteins to DNA, and the cells were lysed in 1.5-ml lysis buffer (50 mM HEPES, pH 7.5, 140 mM NaCl; 1 mM EDTA; 1% Triton X-100; 0.1% sodium deoxy cholate; 0.1% sodium dodecyl sulfate). Cell lysates were sonicated at 2 seconds on/15 seconds off for 3 rounds using a Bioruptor ultrasonic cell disruptor (Diagenode) to shear genomic DNA to an average fragment size of 150 to 250 bp. Of the sample, 1% was removed for use as an input control. ChIP was performed according to the protocol provided by the Simple Chip Enzymatic Chromatin IP Kit (Cell Signaling Technology) using antibodies to pCREB (Cell Signaling Technology). Anti-RNA polymerase II and control IgG were used as positive and negative controls, respectively. After washing and de-crosslinking, the precipitated DNA was purified using a QIAquick PCR purification kit (Qiagen).

ChIP-quantitative PCR. ChIP-quantitative PCR (qPCR) was performed using SYBR green PCR Master Mix and 7900 HT Fast Real-Time PCR System (Applied Biosystems). Primers for Frag 1, 2, and 3 of periostin were used (see Supplemental Table 1 for primer sequenc-

es). Absolute quantification was performed, and enrichment was expressed as a fraction of the whole-cell extract control.

Preparing total RNA for qRT-PCR. Cells were sorted directly into TRIzol. Total RNA was extracted according to the manufacturer's instructions (Invitrogen). Total RNA was subjected to reverse transcription and then qRT-PCR using SYBR green on a LightCycler 480 (Roche). Primers used in this study are listed in Supplemental Table 2.

In vitro assays for migration of PDCs. We assessed cell migration in 96-well Transwell plates (Corning) with 8-μm pore filters. Briefly, we seeded 1×10^4 PDCs/well in the upper chambers and preincubated them with either vehicle, 20-μM AG1296 (a PDGFR inhibitor; Cayman Chemical), 30-μM LY294002 (a PI3K inhibitor; Cayman Chemical), 10-μM MK2206 (an Akt inhibitor; Selleckchem), or 200-nM 666-15 (a CREB inhibitor; R&D Systems) for 1 hour. Then, we incubated them with conditioned medium added with PDGF-BB in the lower chambers for an additional 4 hours, with the inhibitor or vehicle remained in the upper chambers. At the end of incubation, we fixed the cells with 10% formaldehyde for 30 minutes and then removed the cells on the upper surface of each filter with cotton swabs. In certain experiments, we precoated periostin (recombinant mouse periostin/OSF-2 protein; 2955-F2, R&D Systems) on the lower surface of the upper chamber and incubated PDCs with PDGF-BB in the lower chambers. We stained the cells that had migrated through the pores to the lower surface with crystal violet (MilliporeSigma) and quantified them by counting 5 random fields per well using a microscope (Olympus) at ×200 magnification.

Characterization of PDCs. Periosteal stem/progenitor cells were harvested from the periosteum of 1- or 3-month-old *Nestin-GFP* mice or *LepR-cre R26R-EYFP* mice. Nestin-GFP$^+$ Pdgfr-α$^+$ CD45$^-$ CD31$^-$ Ter119$^-$ cells and LepR-YFP$^+$ CD45$^-$ CD31$^-$ Ter119$^-$ cells were sorted by FACS (bone marrow stromal cells sorted by certain cell markers as control). For CFU-F assays with sorted cells, we sorted cells directly into culture at a density of 10 cells/cm^2 in 6-well plates in 3 ml of α-MEM supplemented with glutamine (2 mM), penicillin (100 U/ml), streptomycin sulfate (100 μg/ml), and 20% lot-selected FBS, ensuring that colonies would form at clonal density to allow counting. After 2 to 3 hours of adhesion, unattached cells were removed. On day 10, we fixed and stained the cultures with 0.5% crystal violet. We counted the colonies that contained 50 cells or more. For in vitro differentiation of clonal CFU-F, individual cells were sorted into each well of 48-well plates and cultured for 14 days. Individual CFU-Fs were then digested with 0.25% trypsin/EDTA, split into 3 aliquots, and subcloned into 3 separate cultures permissive for adipocyte, chondrocyte, and osteoblastic differentiation.

For osteogenic differentiation, cells were seeded at a density of 5×10^3/cm^2 with α-MEM supplemented with 10% FBS, 0.1-mM dexamethasone, 10-mM b-glycerol phosphate, and 50-mM ascorbate-2-phosphate. After 3 weeks of differentiation, the mineralization capacity of the cells was evaluated by Alizarin red staining. For adipogenic differentiation, cells were seeded at a density of 1×10^4/cm^2 with α-MEM supplemented with 10% FBS, 1-mM dexamethasone, 0.5-mM 3-isobutyl-1-methylxanthine, and 10 ng/ml^{-1} of insulin for 2 weeks. Lipid accumulation was identified by oil red O staining. For chondrogenic differentiation, cells (1×10^6) were seeded in polypropylene tubes with high-glucose Dulbecco's Modified Eagle Medium (Thermo Fisher Scientific) supplemented with 0.1-mM dexamethasone, 1% insulin-transferrin-sodium selenite mix, 50-mM ascorbate^{-2}-phosphate, 1- mM sodium pyruvate, 50 μg/ml^{-1} of proline, and 20 ng/ml^{-1} of TGF-β3. After 3 weeks in culture, the pellets were fixed in 10% buffered formalin for 2 days and embedded in paraffin. Then, 4-mm-thick sections were processed for toluidine blue staining. The reagents are all commercially available from MilliporeSigma.

To measure in vivo self-renewal capacity of PDCs, we performed a serial cell transplantation experiment. Periosteal Nestin-GFP$^+$PDGFR-α$^+$CD45$^-$ CD31$^-$Ter119$^-$ cells and LepR-YFP$^+$CD45$^-$CD31$^-$Ter119$^-$ cells were sorted by FACS and further cultured for colony formation. We then expanded 1 colony from GFP-labeled periosteal Nestin$^+$ cells or YFP$^+$-labeled periosteal LepR$^+$ cells in 10 μl of α-MEM and injected cells at a density of 1×10^6 per injection into the bone marrow cavity of the left femora of 1-month-old NOD-SCID mice with an immunodeficient background, as previously described (61). GFP$^+$ or YFP$^+$ cells from the bone marrow were collected by FACS 8 weeks after injection and plated for CFU-Fs. The colonies were expanded and retransplanted into the femora of recipient mice for the second round in vivo self-renewal assay. We then sorted GFP$^+$ and YFP$^+$ cells again and cultured these cells to form colonies for analyzing MSC markers CD90 and CD105 by FACS.

Western blots. Approximately 20,000 Nestin-GFP$^+$PDGFR-α$^+$CD45$^-$ CD31$^-$Ter119$^-$ cells were sorted and then resorted into 50 μl of 66% trichloroacetic acid. We incubated extracts on ice for 20 minutes and centrifuged them at 16,100 *g* at 4° for 10 minutes. We then washed precipitates twice in acetone and solubilized the dried pellets in 9-M urea, 2% TritonX-100, and 1% DTT. Samples were separated on 4%–12% Bis-Tris polyacrylamide gels (Invitrogen) and transferred to PVDF membrane (MilliporeSigma). The blots were incubated with primary antibodies overnight at 4°C and then with secondary antibodies. The following primary antibodies were used: p-PDGFR-β (Abcam, ab16868,1:2000), PDGFR-β (Santa Cruz Biotechnology, sc-432, 1:1000), p-PI3K (Cell Signaling Technology, no. 4228, 1:1000), PI3K (Cell Signaling Technology, no. 4292, 1:1000), p-Akt (Cell Signaling Technology, 193H12, 1:1000), Akt (Cell Signaling Technology, 40D4, 1:2000), CREB (Cell Signaling Technology, 48H2, 1:2000), p-CREB (Cell Signaling Technology, 87G3, 1:1000), Periostin (Abcam, ab14041, 1:1000), and GAPDH (Abcam, ab181602, 1:5000).

Statistics. Panels generally represent multiple independent experiments performed on different days with different mice. Data are presented as mean ± SEM unless otherwise stated. Unpaired, 2-tailed Student *t* tests were used for comparisons between 2 groups. For multiple comparisons, 1-way ANOVA with Bonferroni's post hoc test was applied. A *P* value less than 0.05 was deemed significant. All inclusion/exclusion criteria were preestablished, and no samples or animals were excluded from the analysis. The investigators were blinded to allocation during the experiments and outcome assessments. Each animal was assigned an identification number using the animal's litter number in combination with the ear tag number. All data were normally distributed and had similar variation between groups. Statistical analysis was performed using SAS v9.3 software (SAS Institute).

Study approval. We maintained all animals in the animal facility of the Johns Hopkins University School of Medicine (Baltimore, Maryland, USA). The experimental protocols were reviewed and approved by the Institutional Animal Care and Use Committee of the Johns Hopkins University.

Author contributions

XC and BG designed the experiments. BG and RXD carried out most of the experiments. HC, YC, BH, XW, YC, and SFN helped to collect the samples. XC and ZJL supervised the experiments, analyzed the results, and wrote the manuscript. RXD, MW, LY, and SAZ proofread the manuscript.

Acknowledgments

This research was supported by NIH grant AR 071432 (to XC). We thank editors Jenni Weems and Rachel Box for editing the manuscript.

Address correspondence to: Xu Cao, Department of Orthopaedic Surgery, Institute of Cell Engineering, the Johns Hopkins University School of Medicine, 601 North Caroline Street/Suite 5214, Baltimore, Maryland 21287-0881, USA. Phone: 410.502.6440; Email: xcao11@jhmi.edu. Or to: Zhuojing Luo, Institute of Orthopaedic Surgery, Xijing Hospital, Fourth Military Medical University, Xi'an, Shaanxi, 127 Changle Western Road, Xi'an 710032, China. Phone: 8629.84775275; Email: zjluo@fmmu.edu.cn.

1. Orwoll ES. Toward an expanded understanding of the role of the periosteum in skeletal health. *J Bone Miner Res*. 2003;18(6):949–954.
2. Dimitriou R, Tsiridis E, Giannoudis PV. Current concepts of molecular aspects of bone healing. *Injury*. 2005;36(12):1392–1404.
3. Jimenez-Andrade JM, et al. Capsaicin-sensitive sensory nerve fibers contribute to the generation and maintenance of skeletal fracture pain. *Neuroscience*. 2009;162(4):1244–1254.
4. Xie H, et al. PDGF-BB secreted by preosteoclasts induces angiogenesis during coupling with osteogenesis. *Nat Med*. 2014;20(11):1270–1278.
5. Bonnet N, Gineyts E, Ammann P, Conway SJ, Garnero P, Ferrari S. Periostin deficiency increases bone damage and impairs injury response to fatigue loading in adult mice. *PLoS One*. 2013;8(10):e78347.
6. Chen H, et al. Prostaglandin E2 mediates sensory nerve regulation of bone homeostasis. *Nat Commun*. 2019;10(1):181.
7. Chang H, Knothe Tate ML. Concise review: the periosteum: tapping into a reservoir of clinically useful progenitor cells. *Stem Cells Transl Med*. 2012;1(6):480–491.
8. Zhang X, et al. Periosteal progenitor cell fate in segmental cortical bone graft transplantations: implications for functional tissue engineering. *J Bone Miner Res*. 2005;20(12):2124–2137.
9. Nakahara H, Bruder SP, Goldberg VM, Caplan AI. In vivo osteochondrogenic potential of cultured cells derived from the periosteum. *Clin Orthop Relat Res*. 1990;(259):223–232.
10. Colnot C. Skeletal cell fate decisions within periosteum and bone marrow during bone regeneration. *J Bone Miner Res*. 2009;24(2):274–282.
11. Ogita M, Rached MT, Dworakowski E, Bilezikian JP, Kousteni S. Differentiation and proliferation of periosteal osteoblast progenitors are differentially regulated by estrogens and intermittent parathyroid hormone administration. *Endocrinology*. 2008;149(11):5713–5723.
12. Debnath S, et al. Discovery of a periosteal stem cell mediating intramembranous bone formation. *Nature*. 2018;562(7725):133–139.
13. Roberts SJ, van Gastel N, Carmeliet G, Luyten FP. Uncovering the periosteum for skeletal regeneration: the stem cell that lies beneath. *Bone*. 2015;70:10–18.
14. Duchamp de Lageneste O, et al. Periosteum contains skeletal stem cells with high bone regenerative potential controlled by Periostin. *Nat Commun*. 2018;9(1):773.
15. Murao H, Yamamoto K, Matsuda S, Akiyama H. Periosteal cells are a major source of soft callus in bone fracture. *J Bone Miner Metab*. 2013;31(4):390–398.
16. Ferretti C, et al. Human periosteal derived stem cell potential: the impact of age. *Stem Cell Rev*. 2015;11(3):487–500.
17. Uematsu K, Nagata M, Kawase T, Suzuki K, Takagi R. Application of stem-cell media to explant culture of human periosteum: An optimal approach for preparing osteogenic cell material. *J Tissue Eng*. 2013;4:2041731413509646.
18. Evans SF, Docheva D, Bernecker A, Colnot C, Richter RP, Knothe Tate ML. Solid-supported lipid bilayers to drive stem cell fate and tissue architecture using periosteum derived progenitor cells. *Biomaterials*. 2013;34(8):1878–1887.
19. Lim SM, Choi YS, Shin HC, Lee CW, Kim DI. Isolation of human periosteum-derived progenitor cells using immunophenotypes for chondrogenesis. *Biotechnol Lett*. 2005;27(9):607–611.
20. Roberts SJ, Geris L, Kerckhofs G, Desmet E, Schrooten J, Luyten FP. The combined bone forming capacity of human periosteal derived cells and calcium phosphates. *Biomaterials*. 2011;32(19):4393–4405.
21. De Bari C, et al. Mesenchymal multipotency of adult human periosteal cells demonstrated by single-cell lineage analysis. *Arthritis Rheum*. 2006;54(4):1209–1221.
22. Koshihara Y, Hirano M, Kawamura M, Oda H, Higaki S. Mineralization ability of cultured human osteoblast-like periosteal cells does not decline with aging. *J Gerontol*. 1991;46(5):B201–B206.
23. Chan CKF, et al. Identification of the human skeletal stem cell. *Cell*. 2018;175(1):43–56.e21.
24. Méndez-Ferrer S, et al. Mesenchymal and haematopoietic stem cells form a unique bone marrow niche. *Nature*. 2010;466(7308):829–834.
25. Isern J, et al. The neural crest is a source of mesenchymal stem cells with specialized hematopoietic stem cell niche function. *Elife*. 2014;3:e03696.
26. Ono N, Ono W, Mizoguchi T, Nagasawa T, Frenette PS, Kronenberg HM. Vasculature-associated cells expressing nestin in developing bones encompass early cells in the osteoblast and endothelial lineage. *Dev Cell*. 2014;29(3):330–339.
27. Matsuzaki Y, Mabuchi Y, Okano H. Leptin receptor makes its mark on MSCs. *Cell Stem Cell*. 2014;15(2):112–114.
28. Zhou BO, Yue R, Murphy MM, Peyer JG, Morrison SJ. Leptin-receptor-expressing mesenchymal stromal cells represent the main source of bone formed by adult bone marrow. *Cell Stem Cell*. 2014;15(2):154–168.
29. Allen MR, Hock JM, Burr DB. Periosteum: biology, regulation, and response to osteoporosis therapies. *Bone*. 2004;35(5):1003–1012.
30. Seeman E. Periosteal bone formation — a neglected determinant of bone strength. *N Engl J Med*. 2003;349(4):320–323.
31. Rogers HJ. Concentration and distribution of polysaccharides in human cortical bone and the dentine of teeth. *Nature*. 1949;164(4171):625.
32. Turvey ST, Green OR, Holdaway RN. Cortical growth marks reveal extended juvenile development in New Zealand moa. *Nature*. 2005;435(7044):940–943.
33. Genant HK, et al. Noninvasive assessment of bone mineral and structure: state of the art. *J Bone Miner Res*. 1996;11(6):707–730.
34. Vico L, et al. Effects of long-term microgravity exposure on cancellous and cortical weight-bearing bones of cosmonauts. *Lancet*. 2000;355(9215):1607–1611.
35. Wittmers LE, Aufderheide AC, Wallgren J, Rapp G, Alich A. Lead in bone. IV. Distribution of lead in the human skeleton. *Arch Environ Health*. 1988;43(6):381–391.
36. Nalla RK, Kinney JH, Ritchie RO. Mechanistic fracture criteria for the failure of human cortical bone. *Nat Mater*. 2003;2(3):164–168.
37. Matkovic V. Calcium and peak bone mass. *J Intern Med*. 1992;231(2):151–160.
38. Sakagami N, et al. Reduced osteoblastic population and defective mineralization in osteopetrotic (op/op) mice. *Micron*. 2005;36(7-8):688–695.
39. Sinder BP, Pettit AR, McCauley LK. Macrophages: their emerging roles in bone. *J Bone Miner Res*. 2015;30(12):2140–2149.
40. Gosselin D, et al. Environment drives selection and function of enhancers controlling tissue-specific macrophage identities. *Cell*. 2014;159(6):1327–1340.
41. Stefater JA, Ren S, Lang RA, Duffield JS. Metchnikoff's policemen: macrophages in development, homeostasis and regeneration. *Trends Mol Med*. 2011;17(12):743–752.
42. Lawson MA, et al. Osteoclasts control reactivation of dormant myeloma cells by remodelling the endosteal niche. *Nat Commun*. 2015;6:8983.
43. Mansour A, Abou-Ezzi G, Sitnicka E, Jacobsen SE, Wakkach A, Blin-Wakkach C. Osteoclasts promote the formation of hematopoietic stem cell niches in the bone marrow. *J Exp Med*. 2012;209(3):537–549.
44. Zhu S, et al. Subchondral bone osteoclasts induce sensory innervation and osteoarthritis pain. *J Clin Invest*. 2019;129(3):1076–1093.
45. Wang X, et al. Aberrant TGF-β activation in bone tendon insertion induces enthesopathy-like disease. *J Clin Invest*. 2018;128(2):846–860.
46. Zhen G, et al. Inhibition of TGF-β signaling in mesenchymal stem cells of subchondral bone attenuates osteoarthritis. *Nat Med*. 2013;19(6):704–712.
47. Pixley FJ, Stanley ER. CSF-1 regulation of the wandering macrophage: complexity in action. *Trends Cell Biol*. 2004;14(11):628–638.
48. Chen W, et al. Novel pycnodysostosis mouse model uncovers cathepsin K function as a potential regulator of osteoclast apoptosis and senescence. *Hum Mol Genet*. 2007;16(4):410–423.
49. Lin Z, Fateh A, Salem DM, Intini G. Periosteum:

biology and applications in craniofacial bone regeneration. *J Dent Res*. 2014;93(2):109–116.
50. Bonnet N, Brun J, Rousseau JC, Duong LT, Ferrari SL. Cathepsin K controls cortical bone formation by degrading periostin. *J Bone Miner Res*. 2017;32(7):1432–1441.
51. Kashima TG, et al. Periostin, a novel marker of intramembranous ossification, is expressed in fibrous dysplasia and in c-Fos-overexpressing bone lesions. *Hum Pathol*. 2009;40(2):226–237.
52. Bonnet N, Conway SJ, Ferrari SL. Regulation of beta catenin signaling and parathyroid hormone anabolic effects in bone by the matricellular protein periostin. *Proc Natl Acad Sci U S A*. 2012;109(37):15048–15053.
53. Dobbins DE, Sood R, Hashiramoto A, Hansen CT, Wilder RL, Remmers EF. Mutation of macrophage colony stimulating factor (Csf1) causes osteopetrosis in the tl rat. *Biochem Biophys Res Commun*. 2002;294(5):1114–1120.
54. Loureiro RM, et al. csf1 is required for early embryonic macrophage development: characterization of the csf1(op)/csf1(op) mutation in ES cell-derived macrophages. *Br J Haematol*. 2008;141(5):739–742.
55. Ding G, Zhao J, Jiang D. Allicin inhibits oxidative stress-induced mitochondrial dysfunction and apoptosis by promoting PI3K/AKT and CREB/ERK signaling in osteoblast cells. *Exp Ther Med*. 2016;11(6):2553–2560.
56. Kim JM, et al. An activator of the cAMP/PKA/CREB pathway promotes osteogenesis from human mesenchymal stem cells. *J Cell Physiol*. 2013;228(3):617–626.
57. Dossa T, et al. Osteoclast-specific inactivation of the integrin-linked kinase (ILK) inhibits bone resorption. *J Cell Biochem*. 2010;110(4):960–967.
58. Saftig P, et al. Impaired osteoclastic bone resorption leads to osteopetrosis in cathepsin-K-deficient mice. *Proc Natl Acad Sci U S A*. 1998;95(23):13453–13458.
59. Wu X, et al. Inhibition of Sca-1-positive skeletal stem cell recruitment by alendronate blunts the anabolic effects of parathyroid hormone on bone remodeling. *Cell Stem Cell*. 2010;7(5):571–580.
60. Xian L, et al. Matrix IGF-1 maintains bone mass by activation of mTOR in mesenchymal stem cells. *Nat Med*. 2012;18(7):1095–1101.
61. Tang Y, et al. TGF-β1-induced migration of bone mesenchymal stem cells couples bone resorption with formation. *Nat Med*. 2009;15(7):757–765.